Journal of Computational Physics 430 (2021) 110091

Contents lists available at ScienceDirect

Journal of Computational Physics

www.elsevier.com/locate/jcp

General synthetic iterative scheme for nonlinear gas kinetic simulation of multi-scale rarefied gas flows

Lianhua Zhu [a,1], Xingcai Pi [b,1], Wei Su [c], Zhi-Hui Li [b,d], Yonghao Zhang [c], Lei Wu [e,*]

[a] James Weir Fluids Laboratory, Department of Mechanical and Aerospace Engineering, University of Strathclyde, Glasgow G1 1XJ, UK
[b] Hypervelocity Aerodynamics Institute, China Aerodynamics Research and Development Center, Mianyang 621000, China
[c] School of Engineering, University of Edinburgh, Edinburgh EH9 3FB, UK
[d] National Laboratory of Computational Fluid Dynamics, Beijing 100191, China
[e] Department of Mechanics and Aerospace Engineering, Southern University of Science and Technology, Shenzhen 518055, China

ARTICLE INFO

Article history:
Available online 29 December 2020

Keywords:
Gas kinetic equation
Multi-scale rarefied gas flows
Fourier stability analysis
General synthetic iterative scheme
Fast convergence

ABSTRACT

The general synthetic iterative scheme (GSIS) is extended to find the steady-state solution of the nonlinear gas kinetic equation, resolving the long-standing problems of slow convergence and requirement of ultra-fine grids in near-continuum flows. The key ingredient of GSIS is the tight coupling of gas kinetic and macroscopic synthetic equations, where the constitutive relations explicitly contain Newton's law of shear stress and Fourier's law of heat conduction. The higher-order constitutive relations describing rarefaction effects are calculated from the velocity distribution function; however, their constructions are simpler than our previous work (Su et al., 2020 [28]) for linearized gas kinetic equations. On the other hand, solutions of macroscopic synthetic equations are used to accelerate the evolution of gas kinetic equation at the next iteration step. A rigorous linear Fourier stability analysis of the present schemes in periodic system shows that the error decay rate of GSIS can be smaller than 0.5, which means that the deviation to steady-state solution can be reduced by 3 orders of magnitude in 10 iterations. Other important advantages of the GSIS are: (i) it does not rely on the specific form of Boltzmann collision operator, and (ii) it can be solved by sophisticated techniques in computational fluid dynamics, making it amenable to large scale engineering applications. In this paper, the efficiency and accuracy of GSIS are demonstrated by a number of canonical test cases in rarefied gas dynamics, covering different flow regimes.

1. Introduction

Multi-scale rarefied gas flow exists in many engineering applications, ranging from the aerodynamics of re-entering vehicles up in the space to the shale gas transport deep into the underground, including the aerodynamic design of reusable vehicles, aerothermodynamics problems during reentry disintegration of large-scale uncontrolled spacecraft [1,2]. Due to the significant variation of gas density or characteristic length scale, these flows can span several regimes, e.g., the continuum,

* Corresponding author.
E-mail address: wul@sustech.edu.cn (L. Wu).
[1] Both authors contributed equally.

https://doi.org/10.1016/j.jcp.2020.110091
0021-9991/

slip, transition, and free molecular flow regimes, which are usually categorized by the Knudsen number (Kn, the ratio between the mean free path of gas molecules and the characteristic flow length). Gas flow in the continuum regime ($Kn < 0.001$) can be modeled by the Navier-Stokes-Fourier (NSF) equations. But for rarefied flows ($Kn > 0.001$), the NSF equations are inaccurate due to the failure of linear constitutive relations given by Newton's law of shear stress and Fourier's law of heat conduction. To model rarefied gas flows that deviate far from thermodynamic equilibrium, the Boltzmann equation, which is an integral-differential equation describing the evolution of one-particle velocity distribution function (VDF) at the mesoscopic scale, should be used [3]. Although various higher-order macroscopic equations have been derived from the Boltzmann equation, using the Chapman-Enskog expansion or Grad's moment method [4–6], none of them are valid for highly rarefied gas flows.

The common numerical methods for rarefied gas flow simulations are the discrete velocity method (DVM) [7] and the direct simulation Monte Carlo (DSMC) method [8]. In DVM, the Boltzmann equation is first discretized in the velocity and spatial spaces, and then solved deterministically using the computational fluid dynamics (CFD) techniques. In DSMC, simulation particles are used to mimic the streaming and collision of real gas molecules. It has been proven that DSMC solves the Boltzmann equation for monatomic gas when the number of simulated particles tends to be infinite [9,10]. The high-dimensional nature of the Boltzmann equation means that it is much more expensive to be solved compared to the NSF equations. For example, DVM requires appropriate discretization of the velocity space, and DSMC needs a large number of repeated samples, which lead to expensive computational cost. In particular, for low-Kn flows, DSMC becomes prohibitive due to the requirement that the cell size and time step should be respectively smaller than the mean free path and the mean collision time, in order to keep the numerical dissipation small [8]. The conventional DVM also suffers from the same problem due to the decoupled treatment of molecular collision and streaming [11,12].

The failure of NSF equations for rarefied gas flows and the difficulty in solving the Boltzmann equation for near continuum flows make the multiscale simulation challenging. Numerous efforts have been devoted to bridging the gap of macroscopic and mesoscopic methods. The popular approach is to couple the macroscopic and mesoscopic models under the domain-decomposition framework. For example, the CFD-DSMC hybrid approach [13–17] couples the macroscopic and mesoscopic models, which are applied in the continuum and rarefied flow regions, respectively. The implementation of such hybrid approaches usually involves a buffer region where both macroscopic and mesoscopic models are solved and assumed to be valid. In reality, however, these methods face the dilemma of ensuring the validity of NSF equations and the efficiency of mesoscopic methods in the coupling region. Recently, a hybrid approach applying the regularized 26-moment equations rather than the NSF equations in macroscopic regions is proposed, which can significantly relocate the buffer zone towards rarefied flow regions and hence reduces the iteration number for gas kinetic simulations [18].

An alternative approach is to solve gas kinetic equations in the whole computational domain and use appropriate numerical schemes to remove the restrictions on cell size and time step. By coupling the molecular collision and streaming, the unified gas kinetic scheme (UGKS) and its variants [19–23] are able to obtain accurate results when the numerical cell size is much larger than the mean free path λ (in the near-continuum flow regime, the cell size can be at the order of $\lambda\sqrt{Kn}$ in the bulk region) [24]. The implicit version of UGKS further reduces the number of iteration steps [25–27]. The recently-developed general synthetic iterative scheme (GSIS) is also one of these promising multiscale methods [28]. It is a generalization of the synthetic iterative scheme that is originally developed for solving radiation transport equation in the optical thick regions [29] and extended to some special linear rarefied gas flows [30–36]. The GSIS extends the synthetic iterative scheme to general rarefied gas flows, and it is not limited to simple flows where the velocity must be perpendicular to the computational domain. The efficiency and accuracy of GSIS is demonstrated in solving two-dimensional (2D) linearized gas kinetic equationsin the whole flow regime [28,37], where the linearized gas kinetic equation and macroscopic synthetic equations are solved on the same grid alternately, and converged solutions are found within a few dozens of iteration steps. In each iteration of gas kinetic equation, the latest macroscopic quantities from the previous solution of macroscopic synthetic equations are used to evaluate the equilibrium distribution function. While in the macroscopic synthetic equations, expressions of shear stress and heat flux explicitly include the constitutive laws at the first-order of Kn, i.e. Newton's law and Fourier's law; the higher-order contributions are directly calculated by taking the velocity moments of VDF [28]. Compared with other multiscale methods [25,38], GSIS does not rely on specific forms of the Boltzmann collision operator [28]. In addition, sophisticated CFD techniques can be directly used to solve the gas kinetic equation and macroscopic synthetic equations. For example, in the linearized GSIS, the DVM is solved by the upwind method, while the SIMPLE algorithm or discontinuous Galerkin method is used to solve the linearized NSF equations with high-order constitutive relations treated as source terms [28].

It is the aim of this paper to extend the GSIS to solve nonlinear gas kinetic equations and demonstrate its potential for practical applications. The overall framework of the linear GSIS will remain unchanged, i.e., we solve the macroscopic synthetic equations and the nonlinear gas kinetic equation alternately in the whole computational domain. Here, we propose a new way to construct the nonlinear macroscopic synthetic equations, which are solved by compressible CFD techniques. In this paper we use the Shakhov model equation [39] as example, but the method can be used to solve the full BE and other model equations straightforwardly, just as we have achieved in the linear GSIS [28].

The remainder of this paper is organized as follows. In Section 2, we introduce the Shakhov model equation, the convention iterative scheme (CIS) to find the steady-state solutions and its convergence rate. In Section 3, the GSIS for nonlinear gas kinetic equation is constructed, and its convergence rate is rigorously calculated based on the Fourier stability analysis. In Section 4, the numerical schemes for solving both the gas kinetic and macroscopic equations are presented. In Section 5,

several canonical rarefied gas flow problems are carried out to assess the accuracy and efficiency of the nonlinear GSIS. Section 6 concludes with final comments and outlook.

2. Gas kinetic equation, CIS and its convergence rate

2.1. Gas kinetic equation

In gas kinetic theory, the gas dynamics is described by the molecular VDF $f(t,\vec{r},\vec{\xi})$, which depends on the time t, the spatial location $\vec{r}=(x,y,z)$, and the molecular velocity $\vec{\xi}=(\xi_x,\xi_y,\xi_z)$. Evolution of the VDF is governed by the Boltzmann equation:

$$\frac{\partial f}{\partial t}+\vec{\xi}\cdot\vec{\nabla}f=\mathcal{Q}(f), \tag{1}$$

where $\vec{\nabla}$ is the spatial gradient operator and $\mathcal{Q}(f)$ is the collision operator; they describe the change of VDF due to the free streaming and binary collision of gas molecules. Since the Boltzmann collision operator is a complicated five-fold integral, it is usually simplified by the Shakhov model [39]:

$$\mathcal{Q}^s(f)=\frac{f^s(t,\vec{r},\vec{\xi})-f(t,\vec{r},\vec{\xi})}{\tau(t,\vec{r})}, \tag{2}$$

where $\tau=\mu/p$ is the mean collision time, with μ being the shear viscosity and p the pressure of gas. In this paper, we assume the viscosity varies with the temperature T by the power law: $\mu(T)=\mu_0(T/T_0)^{\omega}$, where μ_0 is the reference viscosity at the reference temperature T_0, and ω is a viscosity index. The reference VDF f^s takes the following form:

$$f^s(t,\vec{r},\vec{\xi})=f^m\left[1+(1-\mathrm{Pr})\frac{\vec{q}\cdot\vec{C}}{5pRT}\left(\frac{C^2}{RT}-5\right)\right],\quad f^m=\frac{\rho}{(2\pi RT)^{3/2}}\exp\left(-\frac{C^2}{2RT}\right), \tag{3}$$

where ρ is the mass density, $\vec{U}$ is the macroscopic flow velocity, $\vec{q}$ is the heat flux, $\vec{C}\equiv\vec{\xi}-\vec{U}$ is the peculiar velocity, R is the specific gas constant, and Pr is the Prandtl number. For ideal gas, the equation of state is $p=\rho RT$. The macroscopic variables including the stress tensor σ_{ij} can be calculated by taking moments of the VDF:

$$\begin{aligned}
&\rho(t,\vec{r})=\int f(t,\vec{r},\vec{\xi})\mathrm{d}^3\vec{\xi},\quad \rho\vec{U}(t,\vec{r})=\int f(t,\vec{r},\vec{\xi})\vec{\xi}\mathrm{d}^3\vec{\xi},\\
&\sigma_{ij}(t,\vec{r})=\int f(t,\vec{r},\vec{\xi})C_{\langle i}C_{j\rangle}\mathrm{d}^3\vec{\xi},\quad p(t,\vec{r})=\frac{1}{3}\int f(t,\vec{r},\vec{\xi})C^2\mathrm{d}^3\vec{\xi},\\
&\vec{q}(t,\vec{r})=\frac{1}{2}\int f(t,\vec{r},\vec{\xi})\vec{C}C^2\mathrm{d}^3\vec{\xi},
\end{aligned} \tag{4}$$

where the angle brackets $\langle i,j\rangle$ representing the trace-less part of a tensor, e.g., $a_{\langle i}b_{j\rangle}\equiv a_ib_j-(a_kb_k/3)\delta_{ij}$ with δ_{ij} being the Kronecker delta function.

2.2. The conventional iterative scheme and its efficiency

It is noted that the turbulence is often absent in rarefied gas flows, since the Reynolds is inversely proportional to the Knudsen number. For most practical applications, steady-state solutions of the gas kinetic equation are of particular interest, which can be obtained from CIS by solving the following equation iteratively:

$$\vec{\xi}\cdot\vec{\nabla}f^{k+1}=\frac{1}{\tau^k}[f^{s,k}-f^{k+1}], \tag{5}$$

where k is the step of iteration. Note that in order to avoid solving the nonlinear equation, the reference VDF f_s is calculated from the macroscopic variables of the k-th iteration step, while the VDF f is evaluated at the $(k+1)$-th iteration. The spatial gradient operator can be approximated by the finite difference or discontinuous Galerkin schemes [28,40], and the whole system can be easily solved by sweeping procedures [28,41,42].

We use the Fourier stability analysis to investigate the efficiency of CIS, that is, to see how fast the error decays during iterations. Since the Fourier stability analysis relies on linear systems, we rewrite the collision operator (3) in the following linearized one:

$$f^s=\left[\varrho+2\vec{U}\cdot\vec{\xi}+T\left(\xi^2-\frac{3}{2}\right)+\frac{4}{15}\vec{q}\cdot\vec{\xi}\left(\xi^2-\frac{5}{2}\right)\right]f_{eq}, \tag{6}$$

where the Prandtl number is chosen as 2/3, $f_{eq}=\exp\left(-\xi^2\right)/\pi^{1.5}$ is the global equilibrium VDF, and the macroscopic quantities deviated from their corresponding equilibrium values are:

$$\varrho = \int f \mathrm{d}^3\vec{\xi}, \quad \vec{U} = \int \vec{\xi} f \mathrm{d}^3\vec{\xi}, \quad T = \int \left(\frac{2}{3}\xi^2 - 1\right) f \mathrm{d}^3\vec{\xi},$$
$$\sigma_{ij} = 2\int \xi_{\langle i}\xi_{j\rangle} f \mathrm{d}^3\vec{\xi}, \quad \vec{q} = \int \vec{\xi}\left(\xi^2 - \frac{5}{2}\right) f \mathrm{d}^3\vec{\xi}. \tag{7}$$

Note that after linearization the mean collision time τ in Eq. (2) is a constant, which has the meaning of Knudsen number. More details can be found in Ref. [28].

We define the error functions between VDFs at two consecutive iterations as:

$$Y^{k+1}(\vec{r},\vec{\xi}) = f^{k+1}(\vec{r},\vec{\xi}) - f^{k}(\vec{r},\vec{\xi}), \tag{8}$$

and the error functions for macroscopic quantities $M = [\varrho, \vec{U}, T, \vec{q}]$ between two consecutive iteration steps:

$$\Phi^{k+1}(\vec{r}) = M^{k+1}(\vec{r}) - M^{k}(\vec{r}) = \int Y^{k+1}(\vec{r},\vec{\xi})\phi(\vec{\xi})\mathrm{d}^3\vec{\xi}, \tag{9}$$

where

$$\phi(\vec{\xi}) = \left[1, \xi_x, \xi_y, \frac{2}{3}\xi^2 - 1, \xi_x\left(\xi^2 - \frac{5}{2}\right), \xi_y\left(\xi^2 - \frac{5}{2}\right)\right]. \tag{10}$$

To determine the error decay rate e we perform the Fourier stability analysis by seeking the eigenfunctions $\bar{Y}(\vec{\xi})$ and $\alpha = [\alpha_\varrho, \vec{\alpha}_U, \alpha_T, \vec{\alpha}_q]$ of the following forms:

$$Y^{k+1}(\vec{r},\vec{\xi}) = e^k \bar{Y}(\vec{\xi})\exp(i\vec{\theta}\cdot\vec{r}),$$
$$\Phi^{k+1}(\vec{r}) = e^{k+1}\alpha\exp(i\vec{\theta}\cdot\vec{r}), \tag{11}$$

where i is the imaginary unit and $\vec{\theta} = (\theta_x, \theta_y, \theta_z)$ is the wave vector of perturbance satisfying $|\vec{\theta}| = 1$. The slow convergence occurs when the error decay rate $|e|$ approaches one, where the error is nearly the same when compared to that in the previous iteration. The fast convergence is realized when $|e| < 1$ and approaches zero.

The convective operator in Eq. (5) is kept intact when calculating the error decay rate; the convergence rate of the spatially-discretized gas kinetic equation will be shown in numerical simulations in Section 5. Obviously, from Eqs. (9) and (11) we have

$$e\alpha = \int \bar{Y}(\vec{\xi})\phi(\vec{\xi})\mathrm{d}^3\vec{\xi}, \tag{12}$$

and from Eqs. (5), (6), (8), and (11), we obtain the following expressions for $\bar{Y}(\vec{\xi})$:

$$\bar{Y}(\vec{\xi}) = \frac{\alpha_\varrho + 2\vec{\alpha}_U\cdot\vec{\xi} + \alpha_T\left(\xi^2 - \frac{3}{2}\right) + \frac{4}{15}\vec{\alpha}_q\cdot\vec{\xi}\left(\xi^2 - \frac{5}{2}\right)}{1 + i\tau\vec{\theta}\cdot\vec{\xi}} f_{\mathrm{eq}}. \tag{13}$$

Finally, multiplying Eq. (13) with $\phi(\vec{\xi})$ and integrating the resultant equations with respect to $\vec{\xi}$, we obtain 8 linear algebraic equations for 8 unknown elements in α with the help of Eq. (12). These algebraic equations can be written in the matrix form as

$$C_8\alpha^\top = e\alpha^\top, \tag{14}$$

where the superscript $\top$ is the transpose operator. The error decay rate can be obtained by numerically computing the eigenvalues of matrix C_8 and taking the maximum absolute value of e; the result as a function of the Knudsen number is shown in Fig. 1. It is clear that when the Knudsen number τ is large, e goes to zero so that the error decays quickly. This means that CIS is very efficient for highly rarefied gas flows. On the other hand, $e \to 1$ when $\tau \to 0$, which means that it is hard to obtain converged solutions by using CIS in the near-continuum flow regime.

3. The general synthetic iterative scheme

The GSIS uses the following strategy to accelerate the iteration of conventional DVM schemes for gas kinetic equations [28]: on top of the CIS, it adds macroscopic synthetic equations to boost the convergence to steady-state solutions in the near-continuum flow regime. The flowchart of GSIS is presented in Fig. 2: after completing the CIS at the k-th step, the nonlinear macroscopic synthetic equations are solved to the converged state by sophisticated CFD techniques, with the boundary conditions and high-order constitutive relations from the CIS. The obtained macroscopic quantities are fed back to the CIS, which provides macroscopic quantities and VDFs for the CIS to execute at the $(k+1)$-th step. The details of constructing nonlinear macroscopic equations for GSIS are given below.

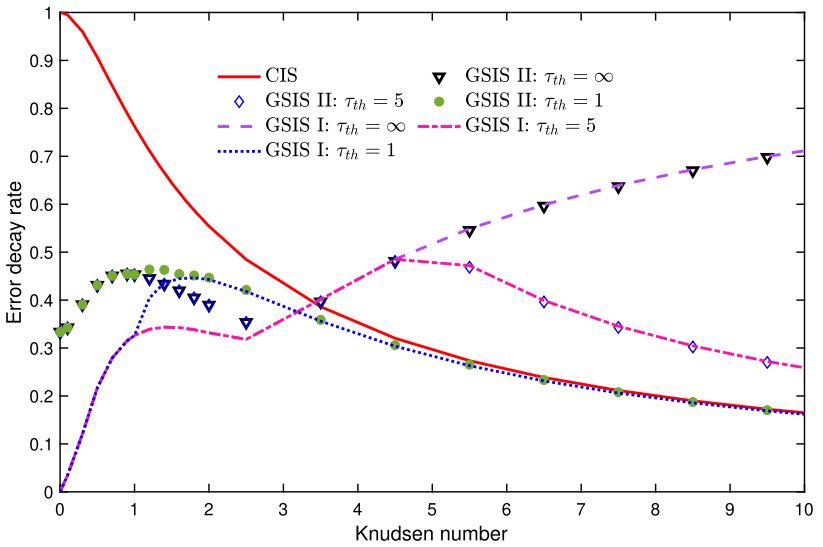

Fig. 1. The error decay rate as a function of the Knudsen number τ in both CIS and GSIS, calculated from the linearized Shakhov model based on the Fourier stability analysis. In GSIS, different threshold Knudsen numbers are considered, see Eq. (27).

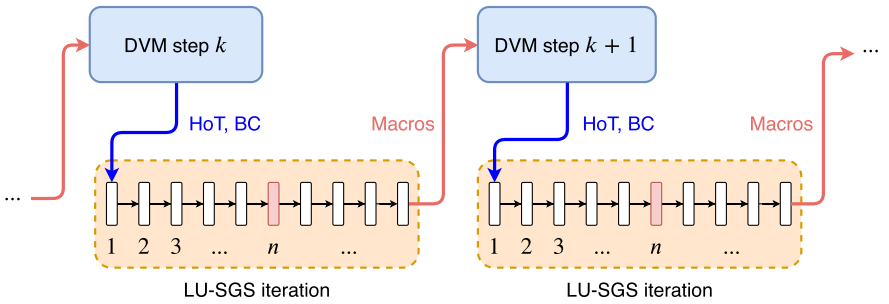

Fig. 2. Flowchart of the computational procedures in GSIS. HoT stands for the high-order terms and BC stands for boundary conditions. LU-SGS is the implicit time-stepping procedure solving the macroscopic synthetic equations after each DVM step.

3.1. Macroscopic synthetic equations

For generality we consider the derivation of macroscopic synthetic equations from the full Boltzmann equation. By multiplying Eq. (1) with 1, $\vec{\xi}$, and ξ^2, and integrating them with respect to $\mathrm{d}^3\xi$, we have:

$$\begin{aligned}
&\frac{\partial \rho}{\partial t}+\vec{\nabla}\cdot(\rho\vec{U})=0,\\
&\frac{\partial \rho\vec{U}}{\partial t}+\vec{\nabla}\cdot(\rho\vec{U}\vec{U})+\vec{\nabla}p+\vec{\nabla}\cdot\boldsymbol{\sigma}=0,\\
&\frac{\partial \rho E}{\partial t}+\vec{\nabla}\cdot\left(\rho E\vec{U}+p\vec{U}+\vec{U}\cdot\boldsymbol{\sigma}+\vec{q}\right)=0,
\end{aligned} \tag{15}$$

where $E=c_vT+U^2/2$ is the total energy with $c_v=3R/2$ being the heat capacity at constant volume. This equation is not closed because the shear stress and heat flux cannot be expressed in terms of the density, velocity and energy. The Chapman-Enskog expansion to the first-order of Knudsen number gives the NSF constitutive relations [3]:

$$\begin{aligned}
&\sigma_{ij}\approx\sigma_{ij,\mathrm{NSF}}=-2\mu\frac{\partial U_{\langle i}}{\partial r_{j\rangle}}=-\mu\left(\frac{\partial U_i}{\partial r_j}+\frac{\partial U_j}{\partial r_i}\right)+\frac{2}{3}\mu\vec{\nabla}\cdot\vec{U}\delta_{ij},\\
&\vec{q}\approx\vec{q}_{\mathrm{NSF}}=-\kappa\vec{\nabla}T,
\end{aligned} \tag{16}$$

where the heat conductivity κ is related to the viscosity and Pr by $\kappa=\mu c_p/\mathrm{Pr}$, with $c_p=5R/2$ being the heat capacity at constant pressure.

However, under rarefied condition, the approximation (16) is not adequate. To be consistent with the gas kinetic equation, the shear stress tensor and heat flux have to be computed from the VDF itself, without any truncation. In the linear

GSIS [28], the shear stress and heat flux used in the macroscopic synthetic equations are expressed in terms of the first-order NSF constitutive relation and higher-order terms (HoTs), where the explicit separation of the NSF constitutive relation out of the diffusive fluxes is essential to achieve fast convergence [43]. Here we do the same for nonlinear GSIS:

$$\begin{aligned}\sigma_{ij} &= \sigma_{ij,\mathrm{NSF}} + \mathrm{HoT}_{\sigma_{ij}},\\ \vec{q} &= \vec{q}_{\mathrm{NSF}} + \mathrm{HoT}_{\vec{q}}.\end{aligned} \tag{17}$$

In the linear GSIS, HoTs are calculated from the spatial derivatives of even higher-order VDF moments than the heat flux and stress tensor [28], which is equivalent to using the governing equations of stress tensor and heat flux in Grad's 13-moment systems but close these moment equations using the VDF from CIS, rather that the one reconstructed using low-order macroscopic quantities. In the nonlinear GSIS here, we can also apply this strategy directly. Multiplying the steady-state kinetic equation with $C_{\langle i}C_{j\rangle}$ and $\vec{C}C^2/2$, and integrating it in the velocity space, we have:

$$\begin{aligned}\sigma^*_{ij} &= \underline{-\frac{\mu^*}{p^*}\int C^*_{\langle i}C^*_{j\rangle}\vec{\xi}\cdot\vec{\nabla}f^*\mathrm{d}^3\vec{\xi}} + \frac{\mu^*}{p^*}\int C^*_{\langle i}C^*_{j\rangle}[\mathcal{Q}(f^*)-\mathcal{Q}^s(f^*)]\mathrm{d}^3\vec{\xi},\\ \vec{q}^{\,*} &= \underline{-\frac{\mu^*}{2p^*\,\mathrm{Pr}}\int \vec{C}^*(C^*)^2\vec{\xi}\cdot\vec{\nabla}f^*\mathrm{d}^3\vec{\xi}} + \frac{\mu^*}{2p^*\,\mathrm{Pr}}\int \vec{C}^*(C^*)^2[\mathcal{Q}(f^*)-\mathcal{Q}^s(f^*)]\mathrm{d}^3\vec{\xi},\end{aligned} \tag{18}$$

where the superscript "*" means that both the VDF and macroscopic quantities are obtained from CIS. It should be noted that the last terms in each equation are much smaller than the corresponding underlined terms. For example, for the Boltzmann collision operator of Maxwell molecules the last term in each equation vanishes [3].

To obtain the HoTs in Eq. (17), we simply subtract the NSF parts from the complete starred stress and heat flux, yielding

$$\begin{aligned}\mathrm{HoT}_{\sigma_{ij}} &= \sigma^*_{ij} - \sigma^*_{ij,\mathrm{NSF}},\\ \mathrm{HoT}_{\vec{q}} &= \vec{q}^{\,*} - \vec{q}^{\,*}_{\mathrm{NSF}},\end{aligned} \tag{19}$$

with the NSF parts $\sigma^*_{ij,\mathrm{NSF}}$ and $\vec{q}^{\,*}_{\mathrm{NSF}}$ calculated from NSF constitutional relations using the starred macroscopic variables. This will be called Scheme I in the following paper.

Alternatively, instead of using the derivatives of higher-order moments to calculate σ^*_{ij} and $\vec{q}^{\,*}$, we can calculate them directly according to their definitions. Then the HoTs are calculated as

$$\begin{aligned}\mathrm{HoT}_{\sigma_{ij}} &= \int f^*C^*_{\langle i}C^*_{j\rangle}\mathrm{d}^3\vec{C}^* - \sigma^*_{ij,\mathrm{NSF}},\\ \mathrm{HoT}_{\vec{q}} &= \frac{1}{2}\int f^*\vec{C}^*(C^*)^2\mathrm{d}^3\vec{C}^* - \vec{q}^{\,*}_{\mathrm{NSF}},\end{aligned} \tag{20}$$

which will be called Scheme II in the following paper.

Remark 1. It is clear that Scheme I is much more complicated than Scheme II, because (i) it involves the calculation of Boltzmann collision operator in the general case and (ii) the underline terms contain spatial derivations which may lead to numerical instabilities around sharp solid corners, while Scheme II does not have this problem. Therefore, if both scheme share the similar value of error decay rate, Scheme II will be used in our numerical simulations. In addition, Scheme II can be directly applied to solve the Boltzmann equations involving multi-species and chemical reactions, where the Scheme I will be extremely complicated.

3.2. Convergence rate of GSIS: scheme II

We analyze the error decay rate of the GSIS based on the linearized Shakhov model and Scheme II; a similar but much simpler analysis for the linearized Bhatnagar–Gross–Krook model is given in Ref. [43]. In GSIS, when f^k is known, f^* is obtained by solving Eq. (5) with $k+1$ replaced by $*$. Then the macroscopic quantities at the $(k+1)$-th iteration step are obtained by solving the following synthetic equations (note that the time derivative is dropped for steady-state solutions):

$$\begin{aligned}&\frac{\partial U_i^{k+1}}{\partial r_i} = 0,\\ &\frac{\partial \varrho^{k+1}}{\partial r_i} + \frac{\partial T^{k+1}}{\partial r_i} + \frac{\partial \sigma_{ij}^{k+1}}{\partial r_j} = 0,\\ &\frac{\partial q_i^{k+1}}{\partial r_i} = 0,\end{aligned} \tag{21}$$

with

$$\begin{aligned}
\sigma_{ij}^{k+1} &= 2\int\left(\xi_i\xi_j - \frac{\xi^2}{3}\delta_{ij}\right) f^* \mathrm{d}^3\vec{\xi} + 2\tau\frac{\partial U_{\langle i}^*}{\partial r_{j\rangle}} - 2\tau\frac{\partial U_{\langle i}^{k+1}}{\partial r_{j\rangle}}, \\
\vec{q}^{\,k+1} &= \int\vec{\xi}\left(\xi^2 - \frac{5}{2}\right) f^* \mathrm{d}^3\vec{\xi} + \frac{15}{8}\tau\vec{\nabla}T^* - \frac{15}{8}\tau\vec{\nabla}T^{k+1},
\end{aligned} \tag{22}$$

which are the linearized version of Eqs. (15), (17) and (20). Therefore, to calculate the convergence rate of GSIS, the error functions in Eqs. (8), (9), and (11) are redefined as

$$\begin{aligned}
Y^*(\vec{r},\vec{\xi}) &= f^*(\vec{r},\vec{\xi}) - f^k(\vec{r},\vec{\xi}) = e^k\bar{Y}(\vec{\xi})\exp(i\vec{\theta}\cdot\vec{r}), \\
\Phi^{k+1}(\vec{r}) &= M^{k+1}(\vec{r}) - M^k(\vec{r}) = e^{k+1}\alpha\exp(i\vec{\theta}\cdot\vec{r}),
\end{aligned} \tag{23}$$

where the solution of $\bar{Y}(\vec{\xi})$ is still given by Eq. (13). Note that the definitions for Φ remain unchanged, but in GSIS they are calculated from the macroscopic synthetic equations, rather than from the VDF Y^*.

With Eqs. (13), (21) (22) and (23), we obtain the following 8 linear algebraic equations for 8 unknowns in α_M:

$$\begin{aligned}
&e(i\theta_x\alpha_{U_x} + i\theta_y\alpha_{U_y} + i\theta_z\alpha_{U_z}) = 0, \\
&e[i\theta_x(\alpha_\varrho + \alpha_T) + \tau\alpha_{u_x}] = S_2, \\
&e[i\theta_y(\alpha_\varrho + \alpha_T) + \tau\alpha_{u_y}] = S_3, \\
&e[i\theta_z(\alpha_\varrho + \alpha_T) + \tau\alpha_{u_z}] = S_4, \\
&e(i\theta_x\alpha_{q_x} + i\theta_y\alpha_{q_y} + i\theta_z\alpha_{q_z}) = 0, \\
&e\left(\frac{15}{8}i\theta_x\tau\alpha_T + \alpha_{q_x}\right) = S_6, \\
&e\left(\frac{15}{8}i\theta_y\tau\alpha_T + \alpha_{q_y}\right) = S_7, \\
&e\left(\frac{15}{8}i\theta_z\tau\alpha_T + \alpha_{q_z}\right) = S_8,
\end{aligned} \tag{24}$$

where the source terms, due to the HoTs in Eq. (22), are also linear functions of α_M:

$$\begin{aligned}
S_2 &= \int\left[\tau\xi_x - 2i\theta_x\left(\xi_x^2 - \frac{\xi^2}{3}\right) - 2i\theta_y\xi_x\xi_y - 2i\theta_z\xi_x\xi_z\right]\bar{Y}(\vec{\xi})\mathrm{d}^3\vec{\xi}, \\
S_3 &= \int\left[\tau\xi_y - 2i\theta_y\left(\xi_y^2 - \frac{\xi^2}{3}\right) - 2i\theta_x\xi_x\xi_y - 2i\theta_z\xi_y\xi_z\right]\bar{Y}(\vec{\xi})\mathrm{d}^3\vec{\xi}, \\
S_4 &= \int\left[\tau\xi_z - 2i\theta_z\left(\xi_z^2 - \frac{\xi^2}{3}\right) - 2i\theta_x\xi_x\xi_z - 2i\theta_y\xi_y\xi_z\right]\bar{Y}(\vec{\xi})\mathrm{d}^3\vec{\xi}, \\
S_6 &= \int\left[\frac{15}{8}i\theta_x\tau\left(\frac{2}{3}\xi^2 - 1\right) + \xi_x\left(\xi^2 - \frac{5}{2}\right)\right]\bar{Y}(\vec{\xi})\mathrm{d}^3\vec{\xi}, \\
S_7 &= \int\left[\frac{15}{8}i\theta_y\tau\left(\frac{2}{3}\xi^2 - 1\right) + \xi_y\left(\xi^2 - \frac{5}{2}\right)\right]\bar{Y}(\vec{\xi})\mathrm{d}^3\vec{\xi}, \\
S_8 &= \int\left[\frac{15}{8}i\theta_z\tau\left(\frac{2}{3}\xi^2 - 1\right) + \xi_z\left(\xi^2 - \frac{5}{2}\right)\right]\bar{Y}(\vec{\xi})\mathrm{d}^3\vec{\xi}.
\end{aligned} \tag{25}$$

The error decay rate of the scheme II can be obtained by solving Eqs. (24) and (25). That is, these equations are firstly rewritten in the matrix form as $L_8 e\alpha^\top = R_8\alpha^\top$, where L_8 and R_8 are two 8×8 matrices. By introducing $G_1 = L_8^{-1}R_8$ and numerically computing its eigenvalues we obtain the error decay rate e of GSIS, see the results in Fig. 1. It is observed that the value of $|e|$ is much reduced when $\tau\to 0$, which demonstrates that the GSIS is able to boost convergence for near-continuum flows. However, the error decay rate increases to one when $\tau\to\infty$.

To fix this problem, macroscopic quantities at the (k+1)-th iteration step are not all updated by the solution M_{syn} from macroscopic synthetic equations, when τ is large. Rather, they are updated in the following manner

$$M^{k+1}(\vec{r}) = \beta M_{\mathrm{syn}} + (1-\beta)M^*(\vec{r}), \tag{26}$$

where the relaxation parameter β is chosen as

$$\beta = \frac{\min(\tau,\tau_{\mathrm{th}})}{\tau}, \tag{27}$$

with τ_{th} being the threshold Knudsen number. That is, $\beta = 1$ when the Knudsen number is smaller than τ_{th}; when $\tau > \tau_{\text{th}}$, β gradually decreases to zero as the Knudsen number approaches infinity. The error decay rate of this GSIS can be obtained by computing the eigenvalue of the matrix $G = \beta L_8^{-1} R_8 + (1-\beta) C_8$, where the results at the threshold Knudsen number of values 1 and 5 are shown in Fig. 1. Clearly, by choosing approximate value of β, we can make the maximum error decay rate less than 0.5 for all Knudsen number; this means that the error can be reduced by at least three orders of magnitude in 10 iterations. Thus, theoretically, GSIS can reach fast convergence in the whole range of Knudsen number.

3.3. Convergence rate of GSIS: scheme I

Schemes I and II differ only in HoTs. Since in Scheme I the shear stress and heat flux for the linearized Shakhov model equation are $\sigma_{ij}^* = -2\tau \int \xi_{\langle i}\xi_{j\rangle}\vec{\xi}\cdot\vec{\nabla} f^* \mathrm{d}^3\vec{\xi}$ and $q_i^* = -\frac{3}{2}\tau \int \xi_i \left(\xi^2 - \frac{5}{2}\right)\vec{\xi}\cdot\vec{\nabla} f^* \mathrm{d}^3\vec{\xi}$, Eq. (25) is modified as

$$
\begin{aligned}
S_2 &= \tau \int \left[\xi_x - 2\Theta(\theta_x \xi_{\langle x\rangle x} + \theta_y \xi_x \xi_y + \theta_z \xi_x \xi_z)\right] \bar{Y}(\vec{\xi})\mathrm{d}^3\vec{\xi},\\
S_3 &= \tau \int \left[\xi_y - 2\Theta(\theta_x \xi_x \xi_y + \theta_y \xi_{\langle y\rangle y} + \theta_z \xi_y \xi_z)\right] \bar{Y}(\vec{\xi})\mathrm{d}^3\vec{\xi},\\
S_4 &= \tau \int \left[\xi_z - 2\Theta(\theta_x \xi_x \xi_z + \theta_y \xi_y \xi_z + \theta_z \xi_{\langle z\rangle z})\right] \bar{Y}(\vec{\xi})\mathrm{d}^3\vec{\xi},\\
S_6 &= i\tau \int \left[\frac{15}{8}\theta_x\left(\frac{2}{3}\xi^2 - 1\right) - \frac{3}{2}\Theta\xi_x\left(\xi^2 - \frac{5}{2}\right)\right] \bar{Y}(\vec{\xi})\mathrm{d}^3\vec{\xi},\\
S_7 &= i\tau \int \left[\frac{15}{8}\theta_y\left(\frac{2}{3}\xi^2 - 1\right) - \frac{3}{2}\Theta\xi_y\left(\xi^2 - \frac{5}{2}\right)\right] \bar{Y}(\vec{\xi})\mathrm{d}^3\vec{\xi},\\
S_8 &= i\tau \int \left[\frac{15}{8}\theta_z\left(\frac{2}{3}\xi^2 - 1\right) - \frac{3}{2}\Theta\xi_z\left(\xi^2 - \frac{5}{2}\right)\right] \bar{Y}(\vec{\xi})\mathrm{d}^3\vec{\xi},
\end{aligned}
\tag{28}
$$

where $\Theta = \theta_x\xi_x + \theta_y\xi_y + \theta_z\xi_z$.

With Eqs. (24), (28), (26) and (27), we obtain the error decay rate of Scheme I, which is also shown in Fig. 1. It is seen that when the Knudsen number $\tau \to 0$, the error decay rate goes to zero, which means that the GSIS with scheme I is very efficient in obtaining the steady-state solution of the gas kinetic equations.

Remark 2. The Fourier stability analysis is conducted in the spatial periodic systems. In reality, however, solid walls are always present, and the Knudsen layer (exists in a region within a few mean free path away from the wall) always makes the effective Knudsen number $\tau \sim 1$. Therefore, the maximum error decay rate in the whole range of Kn is a more important indicator. In this sense, from Fig. 1 we see that schemes I and II have the similar efficacy in boosting the convergence rate to steady-state solutions. We therefore choose Scheme II over Scheme I because it is simpler and can be easily applied to other Boltzmann collision operators.

4. Numerical schemes

4.1. The DVM scheme on curved structured mesh

For irregular computational domain, general structured body-fitted meshes are preferred. In order to use the sophisticated CFD techniques on such meshes, we keep the time derivative in the gas kinetic equation. Using the forward Euler scheme for the time derivative and applying implicit treatment to the convection term and f in the collision term, we have

$$
\frac{f^{k+1} - f^k}{\Delta t} + \vec{\xi}\cdot\vec{\nabla} f^{k+1} = \frac{1}{\tau^k}[f^{s,k} - f^{k+1}],
\tag{29}
$$

which, in order to enable a simple matrix-free implicit solving of the semi-discretized equation, is rewritten in the so-called "delta" form,

$$
\left(\frac{1}{\Delta t} + \frac{1}{\tau^k}\right)\Delta f^k + \vec{\xi}\cdot\vec{\nabla}\Delta f^k = \frac{1}{\tau^k}[f^{s,k} - f^k] - \vec{\xi}\cdot\vec{\nabla} f^k,
\tag{30}
$$

by introducing the incremental VDF $\Delta f^k = f^{k+1} - f^k$.

The gradient operators $\vec{\nabla}$ at the left-hand-side (LHS) and right-hand-side (RHS) of Eq. (30) will be calculated by the first-order upwind scheme and a second-order scheme, respectively [44]. With such a treatment, the implicit part allows a simple matrix-free solving with the Lower-Upper Symmetric Gauss–Seidel (LU-SGS) technique [45], while the converged solution will be second-order accurate.

We apply the finite volume method to solve the above gas kinetic equation. After the volume integration and applying the Gauss theorem, for each cell indexed by (i, j) on a structured grid, we have

$$\left(\frac{1}{\Delta t}+\frac{1}{\tau_{i,j}^{k}}\right)\Omega_{i,j}\Delta f_{i,j}^{k}+\sum_{m}\vec{S}_{m}\cdot\vec{\xi}\,\Delta f_{m}^{k}=\frac{\Omega_{i,j}}{\tau_{i,j}^{k}}(f_{i,j}^{s,k}-f_{i,j}^{k})-\sum_{m}\vec{S}_{m}\cdot\vec{\xi}\,f_{m}^{k}, \tag{31}$$

where $\Omega_{i,j}$ is the cell's volume, m is the index of the faces belonging to the cell, and $\vec{S}_m$ is the face's normal vectors pointing out of the cell with its magnitude being the face area. Variables with subscript i, j are the cell averaged quantities on the cell center, while Δf_m^k and f_m^k are reconstructed variables on the cell faces. For the reconstruction of Δf_m^k, the first-order upwind scheme is applied: at the left face of cell $\Delta f_{i-1/2,j}^k = \Delta f_{i-1,j}^k$ if $\vec{\xi}\cdot\vec{S}_{i-1/2,j} > 0$, otherwise it is $\Delta f_{i-1/2,j}^k = \Delta f_{i,j}^k$. For the reconstruction of f_m^k, various second-order limited interpolation scheme can be applied. In this study, f_m is calculated from the upwind cell center by first-order Taylor expansion, where the slope is calculated with van Leer slope limiter.

With the above discretization, the linear equation system for all cells can be written in the following matrix form,

$$\mathbf{D}_{i,j}\Delta f_{i,j}^{k}+\mathbf{L}_{i,j}^{x}\Delta f_{i-1,j}^{k}+\mathbf{U}_{i,j}^{x}\Delta f_{i+1,j}^{k}+\mathbf{L}_{i,j}^{y}\Delta f_{i,j-1}^{k}+\mathbf{U}_{i,j}^{y}\Delta f_{i,j+1}^{k}=\mathrm{RHS}_{i,j} \tag{32}$$

where the matrix elements are

$$\mathbf{D}_{i,j}=\frac{\Omega_{i,j}}{\Delta t}+\frac{\Omega_{i,j}}{\tau_{i,j}^{k}}+|\vec{S}_{i}\cdot\vec{\xi}|+|\vec{S}_{j}\cdot\vec{\xi}|, \tag{33}$$

$$\mathbf{L}_{i,j}^{x}=\frac{1}{2}\vec{S}_{i}\cdot\vec{\xi}\left[1-\mathrm{sign}(\vec{\xi}\cdot\vec{n}_{i})\right],\quad \mathbf{L}_{i,j}^{y}=\frac{1}{2}\vec{S}_{j}\cdot\vec{\xi}\left[1-\mathrm{sign}(\vec{\xi}\cdot\vec{n}_{j})\right], \tag{34}$$

$$\mathbf{U}_{i,j}^{x}=-\frac{1}{2}\vec{S}_{i}\cdot\vec{\xi}\left[1+\mathrm{sign}(\vec{\xi}\cdot\vec{n}_{i})\right],\quad \mathbf{U}_{i,j}^{y}=-\frac{1}{2}\vec{S}_{j}\cdot\vec{\xi}\left[1+\mathrm{sign}(\vec{\xi}\cdot\vec{n}_{j})\right], \tag{35}$$

with $\vec{n}=\vec{S}/|\vec{S}|$ and $\mathrm{sign}(x)$ the sign function, returns 1 if $x>0$ and -1 otherwise. Here, the approximation $\vec{S}_i = \frac{1}{2}\left(\vec{S}_{i-1/2}+\vec{S}_{i+1/2}\right)\approx\vec{S}_{i-1/2}\approx-\vec{S}_{i+1/2}$ is assumed. By applying the LU-SGS technique to Eq. (32), the incremental VDF is solved by a forward sweeping and a backward sweeping:

$$\text{Forward:}\quad \mathbf{D}_{i,j}\Delta f_{ij}^{*}+\mathbf{L}_{i,j}^{x}\Delta f_{i-1,j}^{*}+\mathbf{L}_{i,j}^{y}\Delta f_{i,j-1}^{*}=\mathrm{RHS}_{ij}, \tag{36}$$

$$\text{Backward:}\quad \Delta f_{ij}^{k}=\Delta f_{ij}^{*}-\mathbf{D}_{i,j}^{-1}\mathbf{U}_{i,j}^{x}\Delta f_{i+1,j}^{*}-\mathbf{D}_{i,j}^{-1}\mathbf{U}_{i,j}^{y}\Delta f_{i,j+1}^{*}, \tag{37}$$

and the VDF is then updated as $f_{i,j}^{k+1}=f_{i,j}^{k}+\Delta f_{i,j}^{k}$.

4.2. Numerical scheme for the macroscopic synthetic equations

The macroscopic synthetic equations (15) can be viewed as the compressible NSF equation with HoTs as constant source terms, where the steady-state solution can be obtained by using sophisticated time-implicit schemes and shock capturing schemes. Again, we use the LU-SGS technique to handle the implicit time stepping in a matrix-free manner.

Integrating Eq. (15) in a control volume Ω of the finite volume mesh and applying the Gauss theorem, we have

$$\frac{\partial}{\partial t}\int_{\Omega}\vec{W}\,\mathrm{d}\Omega+\oint_{\partial\Omega}\left[\vec{F}_{\mathrm{c}}+\vec{F}_{\mathrm{v}}(\boldsymbol{\sigma}_{\mathrm{NSF}},\vec{q}_{\mathrm{NSF}})\right]\mathrm{d}\vec{S}=-\oint_{\partial\Omega}\vec{F}_{\mathrm{v}}^{\mathrm{HoT}}\mathrm{d}\vec{S}, \tag{38}$$

where $\vec{W}$ is the vector of conservative variables and $\vec{F}_{\mathrm{c}}$ is the vector of convective fluxes:

$$\vec{W}=\begin{bmatrix}\rho\\ \rho U_x\\ \rho U_y\\ \rho E\end{bmatrix},\quad \vec{F}_{\mathrm{c}}=\begin{bmatrix}\rho V\\ \rho U_x V+n_x p/2\\ \rho U_y V+n_y p/2\\ \rho H V\end{bmatrix}. \tag{39}$$

Here, $H=E+p/\rho$, $V=\vec{U}\cdot\vec{n}$ with $\vec{n}$ being the unit normal vector of $\mathrm{d}\vec{S}$, and

$$\vec{F}_{\mathrm{v}}(\boldsymbol{\sigma},\vec{q})=\begin{bmatrix}0\\ n_x\sigma_{xx}/2+n_y\sigma_{xy}/2\\ n_x\sigma_{yx}/2+n_y\sigma_{yy}/2\\ n_x\Theta_x(\boldsymbol{\sigma},\vec{q})+n_y\Theta_y(\boldsymbol{\sigma},\vec{q})\end{bmatrix}, \tag{40}$$

where $\mathcal{F}_x(\boldsymbol{\sigma},\vec{q})=-U_x\sigma_{xx}-U_y\sigma_{xy}+q_x$ and $\mathcal{F}_y(\boldsymbol{\sigma},\vec{q})=-U_x\sigma_{yx}-U_y\sigma_{yy}+q_y$. In the RHS of Eq. (38), $\vec{F}_{\mathrm{v}}^{\mathrm{HoT}}\equiv\vec{F}_{\mathrm{v}}(\boldsymbol{\sigma}^{*},\vec{q}*)-\vec{F}_{\mathrm{v}}(\boldsymbol{\sigma}_{\mathrm{NSF}}^{*},\vec{q}_{\mathrm{NSF}}^{*})$ is the viscous flux due to the HoTs in shear stress and heat flux. The starred variables have the same meaning as in Eq. (19).

Applying the implicit scheme for the fluxes at the LHS of Eq. (38), we have, for each cell,

$$\left[\left(\frac{\Omega}{\Delta t_p}\right)_{i,j}\vec{I}+\left(\frac{\partial\vec{R}}{\partial\vec{W}}\right)_{i,j}\right]\Delta\vec{W}^n_{i,j}=-\vec{R}^n_{i,j}+\vec{R}^{\mathrm{HoT}}_{i,j}, \tag{41}$$

where Δt_p is the pseudo time step, $\vec{I}$ is the identity matrix, and $\vec{R}$ stands for the residues including one in the NSF equation and one due to HoTs:

$$\begin{aligned}\vec{R}^n_{i,j}&=\sum_{m\in N(i,j)}[\vec{F}^n_{\mathrm{c}}+\vec{F}_{\mathrm{v}}(\boldsymbol{\sigma}^n_{\mathrm{NSF}},\vec{q}^n_{\mathrm{NSF}})]_m\Delta S_m,\\ \vec{R}^{\mathrm{HoT}}_{i,j}&=\sum_{m\in N(i,j)}(\vec{F}^{\mathrm{HoT}}_{\mathrm{v}})_m\Delta S_m,\end{aligned} \tag{42}$$

with the index m looping through all the faces of the current cell, represented by $N(i,j)$. As the iteration converges ($\Delta\vec{W}^n$ approaches to zero), the RHS of Eq. (41) also approaches to zero.

The LU-SGS technique employs a factorization of the implicit operator in Eq. (41) as

$$(\mathbf{D}+\mathbf{L})\mathbf{D}^{-1}(\mathbf{D}+\mathbf{U})\Delta\vec{W}^n=-\vec{R}^n+\vec{R}^{\mathrm{HoT}}. \tag{43}$$

Note that the symbols **D**, **L** and **U** are different from the ones in the DVM (32). The solution of the linear equation system in terms of $\Delta\vec{W}^n$ can be easily executed as a forward sweep and a backward sweep procedure on a structured mesh [46], as only the lower- or upper-half matrix coefficients are non-zero,

$$\begin{aligned}&\text{Forward:}\quad(\mathbf{D}+\mathbf{L})\Delta\vec{W}^{(1)}=-\vec{R}^n+\vec{R}^{\mathrm{HoT}},\\ &\text{Backward:}\quad(\mathbf{D}+\mathbf{U})\Delta\vec{W}^n=\mathbf{D}\Delta\vec{W}^{(1)},\end{aligned} \tag{44}$$

where, for each cell, the lower, the upper and diagonal matrix elements are:

$$\begin{aligned}\mathbf{L}_{i,j}&=\left(\bar{A}^+_{i-1}+\bar{A}_{\mathrm{v}}\right)_{i-1}\Delta S_{i-1/2}+\left(\bar{A}^+_{j-1}+\bar{A}_{\mathrm{v}}\right)_{j-1}\Delta S_{j-1/2},\\ \mathbf{U}_{i,j}&=\left(\bar{A}^-_{i+1}-\bar{A}_{\mathrm{v}}\right)_{i+1}\Delta S_{i+1/2}+\left(\bar{A}^-_{j+1}-\bar{A}_{\mathrm{v}}\right)_{j+1}\Delta S_{j+1/2},\\ \mathbf{D}_{i,j}&=\frac{\Omega}{\Delta t}\mathbf{I}+\left(\bar{A}^-_{i-1/2}-\bar{A}_{\mathrm{v}}\right)\Delta S_{i-1/2}+\left(\bar{A}^-_{j-1/2}-\bar{A}_{\mathrm{v}}\right)\Delta S_{j-1/2}\\ &\quad+\left(\bar{A}^+_{i+1/2}+\bar{A}_{\mathrm{v}}\right)\Delta S_{i+1/2}+\left(\bar{A}^+_{j+1/2}+\bar{A}_{\mathrm{v}}\right)\Delta S_{j+1/2},\end{aligned} \tag{45}$$

with $\bar{A}^{\pm}$ being the positive and negative convective flux Jacobian due to the flux-vector splitting scheme, and $\bar{A}_{\mathrm{v}}$ the viscous flux Jacobian. During the forward and backward sweeps, the product of convective flux Jacobian and change of conservation variables can be approximated as [46]:

$$(\bar{A}^{\pm}\Delta S)\Delta\vec{W}^n\approx\frac{1}{2}\left(\Delta\bar{F}^n_{\mathrm{c}}\Delta S\pm r_A\bar{I}\Delta\vec{W}^n\right),\quad r_A=w\hat{\Lambda}_{\mathrm{c}}, \tag{46}$$

where ΔF is the change of convective flux due to the change of conservative variables, $\hat{\Lambda}_{\mathrm{c}}$ is the convective flux Jacobian's spectral radius, and w is the over-relaxation factor in the range of $1<w\le 2$. A large w increases the stability but slows down the convergence speed. In this paper, we use $w=1$. Depending on the orientation of the interface (I- or J-direction), $\hat{\Lambda}_{\mathrm{c}}$ is evaluated as

$$\hat{\Lambda}^I_{\mathrm{c}}=(|\vec{U}_{i,j}\cdot\vec{n}_I|+c_{i,j})\Delta S_I\quad\text{and}\quad\hat{\Lambda}^J_{\mathrm{c}}=(|\vec{U}_{i,j}\cdot\vec{n}_J|+c_{i,j})\Delta S_J, \tag{47}$$

where $\vec{n}_I=\left(\vec{n}_{i+1/2,j}+\vec{n}_{i-1/2,j}\right)/2$, $\Delta S_I=\left(\Delta S_{i+1/2,j}+\Delta S_{i-1/2,j}\right)/2$ with $c_{i,j}$ being the sound of speed and $\vec{n}_{i\pm1/2,j}$ being the right/left face normal vector. Similar definition is used for the J-oriented face. The viscous flux Jacobian is approximated by its spectral radius, i.e. $\bar{A}_{\mathrm{v}}\Delta S\approx\hat{\Lambda}_{\mathrm{v}}$, and for the I- or J-oriented faces,

$$\hat{\Lambda}^I_{\mathrm{v}}=\max\left(\frac{4}{3\rho_{i,j}},\frac{\gamma}{\rho_{i,j}}\right)\left(\frac{\mu_{i,j}}{\mathrm{Pr}}\right)\frac{(\Delta S_I)^2}{\Omega_{i,j}},\quad\text{and}\quad\hat{\Lambda}^J_{\mathrm{v}}=\max\left(\frac{4}{3\rho_{i,j}},\frac{\gamma}{\rho_{i,j}}\right)\left(\frac{\mu_{i,j}}{\mathrm{Pr}}\right)\frac{(\Delta S_J)^2}{\Omega_{i,j}}, \tag{48}$$

where $\gamma=c_{\mathrm{p}}/c_{\mathrm{v}}$.

For the explicit calculation of viscous flux in R^n, we use the MUSCL3 reconstruction scheme and 2nd-order Roe flux scheme, while the 2nd-order central scheme is adopted for the viscous flux computation. The time step is determined according to

$$\Delta t_p=\zeta\frac{\Omega}{\hat{\Lambda}^I_c+\hat{\Lambda}^J_c+\hat{\Lambda}^I_v+\hat{\Lambda}^J_v}, \tag{49}$$

where ζ is the Courant-Friedrichs-Lewy (CFL) number.

4.3. Updating of macroscopic variables and correction to the VDF

The converged solution of macroscopic variables of the synthetic equations is used in the next DVM step to calculate the equilibrium VDF. A relaxation coefficient $0 \leq \beta < 1$ is introduced in the updating processes (26) to improve the convergence and stability of GSIS for high Kn flows,

$$\vec{W}^{k+1} = \beta \vec{W}' + (1-\beta)\vec{W}^{k,*}, \quad \boldsymbol{\sigma}^{k+1} = \beta \boldsymbol{\sigma}' + (1-\beta)\boldsymbol{\sigma}^{k,*}, \quad \vec{q}^{k+1} = \beta \vec{q}' + (1-\beta)\vec{q}^{k,*}, \tag{50}$$

where $\vec{W}'$, $\boldsymbol{\sigma}'$ and $\vec{q}$ are the converged macroscopic solution of the inner loop between the k- and $(k+1)$-th DVM steps, and $\vec{W}^{k,*}$, $\boldsymbol{\sigma}^{k,*}$, $\vec{q}^{k,*}$ are calculated by numerical quadratures after k-th DVM step. In the practical numerical simulations, the relaxation coefficient is adapted according to a local NSF breakdown parameter [47]:

$$\beta = 1 - \min(1, E_c^{\mathrm{NSF}}), \quad E_c^{\mathrm{NSF}} = \sqrt{\frac{\int (f - f^{\mathrm{G13}}) \mathrm{d}^3\vec{\xi}}{\int (f^m)^2 \mathrm{d}^3\vec{\xi}}}, \tag{51}$$

where f^{G13} is the VDF reconstructed following the one used in Grad 13-moment method. For continuum flows, E_c^{NSF} approaches to zero and β approaches to 1, which means the macroscopic variables in the DVM are almost entirely replaced by the solution of macroscopic synthetic equations. For high Kn flows, E_c^{NSF} may be higher than 1 and β becomes zero, so the solution of macroscopic synthetic equations is not used in the DVM and the GSIS reduces to CIS which is already efficient for these flows.

The VDF is also adjusted to reflect the changes of leading-order moments $\vec{W}$. This is achieved by replacing the equilibrium part of the VDF with the one computed from the new moments, while keeping the non-equilibrium part:

$$f^{k+1} = f^k + \beta \left[f^m(\vec{W}^{k+1}) - f^m(\vec{W}^{k,*}) \right]. \tag{52}$$

4.4. Overview of the GSIS algorithm

Here, we summarize the proposed GSIS algorithm for nonlinear gas kinetic equation. The overall computing procedure is a nested loop, with the outer and inner loop indexes as k and n, as illustrated in Fig. 2. The outer loop solves the gas kinetic equation using the iterative or time-stepping DVM method, and the inner loop solves the macroscopic synthetic equations using the LU-SGS technique. Each inner loop starts from the latest macroscopic state, together with HoTs and boundary conditions from the current step in the outer loop. The step-by-step procedures are summarized as below,

1. Initialize macroscopic variables in both the DVM and macroscopic equation solvers;
2. Initialize VDF in the DVM solver;
3. Solve the NSF equations (the macroscopic equation with HoTs as zero) to its converged state.
4. Execute one iterate/time step in the DVM solver, in which the latest converged macroscopic variables are used to compute equilibrium;
5. Calculate the HoTs of shear stress and heat flux from VDF via Eq. (20). Calculate the macroscopic boundary conditions from the VDF on the boundaries;
6. Solve the macroscopic synthetic equation (with the HoTs and the boundary conditions from Step 5) using the LU-SGS technique to the converged state;
7. Update the macroscopic variables and VDF in DVM from the solution in Step 6;
8. Repeat the steps 4 to 7 until meeting the defined convergence criterion of the outer loop via Eq. (50) and (52).

5. Numerical test cases

Several 1D and 2D flows are simulated to investigate accuracy and efficiency of the nonlinear GSIS. In the 1D Fourier and Couette flow, the macroscopic synthetic equations can be greatly simplified and solved without resorting to the LU-SGS technique discussed in Sec. 4.2. The 2D cases include the lid-driven cavity flow and the supersonic flow past a cylinder, where the gas kinetic equation is solved by the upwind finite difference method and the method in Section 4.1, respectively. In all the test cases, $\mathrm{Pr} = 2/3$ and the viscosity index ω is 0.81. All the parameters used in the CIS and GSIS simulations are the same, thus we can directly compare their efficiency and accuracy.

5.1. Reduced Shakhov model equation

For 2D flows, the VDF can be reduced to save computational cost. We introduce the following two reduced VDFs as:

$$\begin{aligned} g(t,x,y,\xi_x,\xi_y) &= \int f(t,\vec{r},\vec{\xi})\mathrm{d}\xi_z, \\ h(t,x,y,\xi_x,\xi_y) &= \int \xi_z^2 f(t,\vec{r},\vec{\xi})\mathrm{d}\xi_z, \end{aligned} \tag{53}$$

whose dynamics are described by the following reduced Shakhov model equation:

$$\frac{\partial \Psi}{\partial t} + \vec{\xi} \cdot \vec{\nabla} \Psi = \frac{1}{\tau}(\Psi^s - \Psi), \tag{54}$$

with $\Psi \equiv [g, h]^\top$, $\Psi^s \equiv [g^s, h^s]^\top$, and

$$g^s = \frac{\rho}{2\pi RT} \exp\left(-\frac{C^2}{2RT}\right)\left[1 + (1-\mathrm{Pr})\frac{\vec{q}\cdot\vec{C}}{5pRT}\left(\frac{C^2}{RT} - 4\right)\right], \tag{55}$$

$$h^s = \frac{\rho}{2\pi RT} \exp\left(-\frac{C^2}{2RT}\right)\left[1 + (1-\mathrm{Pr})\frac{\vec{q}\cdot\vec{C}}{5pRT}\left(\frac{C^2}{RT} - 2\right)\right]RT. \tag{56}$$

Note that now all the vectors have only two components, e.g. $\vec{\xi} = (\xi_x, \xi_y)$, $\vec{C} = (C_x, C_y)$, and $C^2 = C_x^2 + C_y^2$. The macroscopic variables are therefore calculated as:

$$\begin{aligned} &\rho = \int g \mathrm{d}^2\vec{\xi}, \quad \rho\vec{U} = \int g\vec{\xi}\mathrm{d}^2\vec{\xi}, \quad \sigma_{ij} = \int \left(gC_iC_j - \frac{gC^2 + h}{3}\delta_{ij}\right)\mathrm{d}^2\vec{\xi}, \\ &p = \frac{1}{3}\int (gC^2 + h)\mathrm{d}^2\vec{\xi}, \quad \vec{q} = \frac{1}{2}\int \vec{C}(gC^2 + h)\mathrm{d}^2\vec{\xi}. \end{aligned} \tag{57}$$

5.2. Heat transfer between two parallel plates

Consider the steady heat transfer of gas confined between two vertically placed static parallel plates located at $x_\mathrm{L} = 0$ and $x_\mathrm{R} = 1$. The left and right plates have constant temperatures of $T_\mathrm{L} = 0.75$ and $T_\mathrm{R} = 1.25$, respectively (note that the temperature has been normalized by the reference temperature T_0). The boundary conditions of the VDF at x_L and x_R are

$$g(\vec{\xi})|_{x_\mathrm{L},\xi_x>0} = \frac{\rho_\mathrm{L}}{2\pi RT_\mathrm{L}} \exp\left(-\frac{\xi^2}{2RT_\mathrm{L}}\right), \quad h(\vec{\xi})|_{x_\mathrm{L},\xi_x>0} = \frac{\rho_\mathrm{L}}{2\pi} \exp\left(-\frac{\xi^2}{2RT_\mathrm{L}}\right), \tag{58a}$$

$$g(\vec{\xi})|_{x_\mathrm{R},\xi_x<0} = \frac{\rho_\mathrm{R}}{2\pi RT_\mathrm{R}} \exp\left(-\frac{\xi^2}{2RT_\mathrm{R}}\right), \quad h(\vec{\xi})|_{x_\mathrm{R},\xi_x<0} = \frac{\rho_\mathrm{R}}{2\pi} \exp\left(-\frac{\xi^2}{2RT_\mathrm{R}}\right), \tag{58b}$$

where

$$\rho_\mathrm{L} = -\frac{4}{\pi\sqrt{2RT_\mathrm{L}}}\int_{\xi_x<0} \xi_x f \mathrm{d}^2\vec{\xi}, \quad \rho_\mathrm{R} = \frac{4}{\pi\sqrt{2RT_\mathrm{R}}}\int_{\xi_x>0} \xi_x g \mathrm{d}^2\vec{\xi}. \tag{59}$$

For this 1D problem, we can easily solve the steady-state synthetic macroscopic equation as follows. We know that $\vec{U} = 0$, $q_y = 0$, $\sigma_{xy} = \sigma_{yx} = 0$, $\partial\phi/\partial y = 0$, where ϕ is any macroscopic quantity. The synthetic equation together with the equation of state for ideal gas can then be simplified to a system of equations for ρ, T, p, σ_{xx} and q_x:

$$\frac{\partial p}{\partial x} + \frac{\partial \sigma_{xx}}{\partial x} = 0, \tag{60a}$$

$$\frac{\partial q_x}{\partial x} = 0, \tag{60b}$$

$$\sigma_{xx} = \mathrm{HoT}_{\sigma_{xx}}, \tag{60c}$$

$$q_x = \mathrm{HoT}_{q_x} - \kappa\frac{\partial T}{\partial x}, \tag{60d}$$

$$p = \rho RT. \tag{60e}$$

The boundary values of the variables are provided after each DVM step. The HoTs are also computed from the VDF according to Eq. (20) after the last DVM step as

$$\mathrm{HoT}_{\sigma_{xx}} = \frac{1}{3}\int \left(2g^*C_x^{*2} - g^*C_y^{*,2} - h^*\right)\mathrm{d}^2\vec{\xi}, \tag{61a}$$

$$\mathrm{HoT}_{q_x} = \frac{1}{2}\int C_x^*\left(g^*C^{*,2} + h^*\right)\mathrm{d}^2\vec{\xi} + \kappa^*\frac{\partial T^*}{\partial x}, \tag{61b}$$

where starred variables including T^*, k^*, and $\vec{C}^* \equiv \vec{\xi} - \vec{U}^*$ are obtained using the VDF of the last DVM step. Equation (60) can be sequentially solved to calculate σ_{xx} using Eq. (60c); q_x, Eq. (60b); T, Eq. (60d); p, Eq. (60a); and ρ, Eq. (60e).

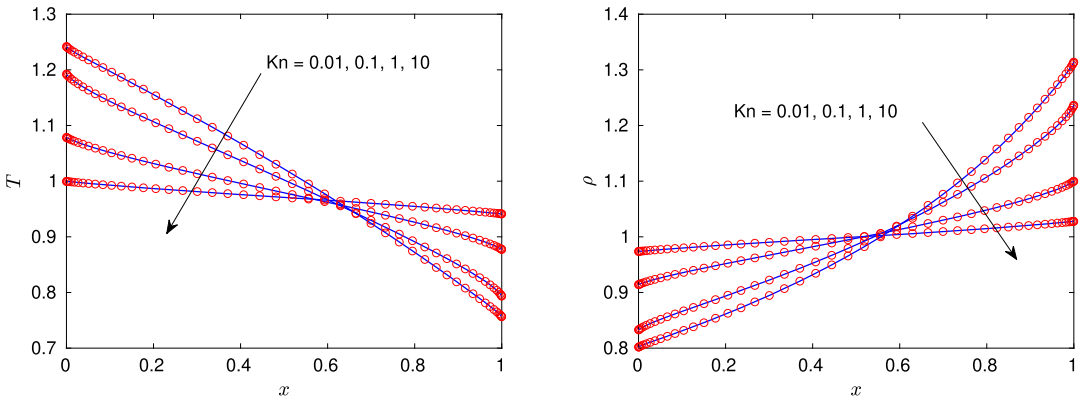

Fig. 3. Temperature (a) and density (b) profiles of the Fourier flow at different Kn. The solid lines and circles represent the CIS and GSIS results, respectively.

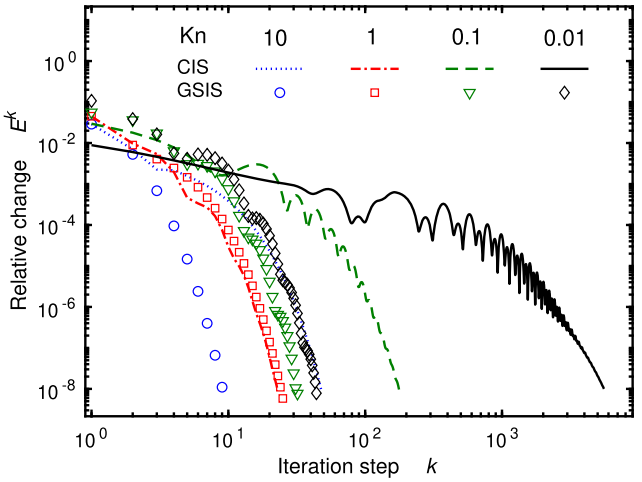

Fig. 4. Convergence history of both GSIS and CIS in the simulation of nonlinear Fourier flow.

The Knudsen number is defined as $\mathrm{Kn} = \sqrt{\pi}\mu C_0/(2p_0L_0)$ with $\mu = \mathrm{Pr}k/c_\mathrm{p}$, where the reference pressure is $p_0 = \rho_0 R T_0 = 0.5$, the reference density is $\rho_0 = 1$, the specific gas constant is $R = 0.5$, the reference temperature is $T_0 = 1$, the reference length $L_0 = x_\mathrm{R} - x_\mathrm{L} = 1$, and the reference velocity $C_0 = \sqrt{2RT_0} = 1$.

The velocity space in both ξ_x and ξ_y directions is truncated to $[-6, 6]$, and the discrete velocities are distributed on a non-uniform Cartesian grid with size of N_V^2, and the grid line positions are determined by the following rule [48]:

$$\xi_x, \xi_y = \frac{6}{(N_\mathrm{v}-1)^3}\left[(-N_\mathrm{v}+1)^3, (-N_\mathrm{v}+3)^3, \cdots, (N_\mathrm{v}-1)^3\right], \tag{62}$$

where $N_V = 32$. Such a non-uniform grid can accurately capture the discontinuity of VDF near the origin of the velocity space, which appears in the vicinity of solid walls when the Knudsen number is large. The spatial grid points are distributed in the x-direction non-uniformly according to the following rule:

$$x_i = s_i^3(10 - 15s_i + 6s_i^2), \quad \text{with} \quad s_i = i/2(N_x - 1), \quad i = 0, 1, \ldots, N_x - 1, \tag{63}$$

where $N_x = 50$ is the number of grid points. The convergence criterion for the DVM iteration is that the volume-weighted relative change of temperature between two successive iterations satisfies

$$E^k = \frac{\sqrt{\sum_i (T_i^k - T_i^{k-1})^2 \Delta x_i}}{\sqrt{\sum_i (T_i^{k-1})^2 \Delta x_i}} < 1 \times 10^{-8}. \tag{64}$$

The temperature field is chosen because it converges slower than other macroscopic fields.

Fig. 3 shows the converged temperature and density profiles calculated by GSIS and CIS. We can see that the results obtained from GSIS agree well with those from CIS. The convergence history of DVM iterations in both GSIS and CIS is

shown in Fig. 4. It is clear that the CIS is efficient in high Kn cases (Kn > 1), where converged solution can be found within 20 iterations. However, it becomes very inefficient when Kn < 0.1, for example, it takes 5,000 iterations to produce the converged solution. On the contrary, GSIS converges in less than 60 steps for the whole Kn range.

5.3. Couette flow

The Couette flow has the same geometry configuration as the Fourier flow, but the two plates have the same temperature of $T_0 = 1$ and different vertical velocities: $U_{y,\mathrm{L}} = -0.25$ and $U_{y,\mathrm{R}} = 0.25$, respectively. The boundary conditions of the VDF at x_L and x_R are

$$g(\vec{\xi})|_{x_\mathrm{L},\xi_x>0} = \frac{\rho_\mathrm{L}}{2\pi RT_0}\exp\left[-\frac{\xi_x^2+(\xi_y-U_{y,\mathrm{L}})^2+\xi_z^2}{2RT_0}\right], \tag{65a}$$

$$h(\vec{\xi})|_{x_\mathrm{L},\xi_x>0} = RT_0 g(\vec{\xi})|_{x_\mathrm{L},\xi_x>0}, \tag{65b}$$

$$g(\vec{\xi})|_{x_\mathrm{R},\xi_x<0} = \frac{\rho_\mathrm{R}}{2\pi RT_0}\exp\left[-\frac{\xi_x^2+(\xi_y-U_{y,\mathrm{R}})^2+\xi_z^2}{2RT_0}\right], \tag{65c}$$

$$h(\vec{\xi})|_{x_\mathrm{R},\xi_x<0} = RT_0 g(\vec{\xi})|_{x_\mathrm{R},\xi_x<0}, \tag{65d}$$

with

$$\rho_\mathrm{L} = -\frac{4}{\pi\sqrt{2RT_\mathrm{L}}}\int_{\xi_x<0}\xi_x f\,\mathrm{d}^2\vec{\xi}, \quad \text{and} \quad \rho_\mathrm{R} = \frac{4}{\pi\sqrt{2RT_\mathrm{R}}}\int_{\xi_x>0}\xi_x f\,\mathrm{d}^2\vec{\xi}. \tag{66}$$

Similar to the Fourier flow, we solve the macroscopic synthetic equations in the following simplified procedure. We know that $U_x = 0$, $q_y = 0$, $\partial\phi/\partial y = 0$, where ϕ can be any flow variable. Thus the synthetic equations can be simplified as a system of equations for ρ, T, p, σ_{xx}, σ_{xy} and q_x:

$$\frac{\partial p}{\partial x} + \frac{\partial \sigma_{xx}}{\partial x} = 0, \tag{67a}$$

$$\frac{\partial \sigma_{xy}}{\partial x} = 0, \tag{67b}$$

$$\frac{\partial \sigma_{xy}U_y}{\partial x} + \frac{\partial q_x}{\partial x} = 0, \tag{67c}$$

$$p = \rho RT, \tag{67d}$$

$$\sigma_{xy} = \mathrm{HoT}_{\sigma_{xy}} - \mu\frac{\partial U_y}{\partial x}, \tag{67e}$$

$$\sigma_{xx} = \mathrm{HoT}_{\sigma_{xx}}, \tag{67f}$$

$$q_x = \mathrm{HoT}_{q_x} - \kappa\frac{\partial T}{\partial x}, \tag{67g}$$

where the HoTs are calculated explicitly according to Eq. (20) as

$$\mathrm{HoT}_{\sigma_{xx}} = \frac{1}{3}\int\left(2g^*C_x^{*,2} - g^*C_y^{*,2} - h^*\right)\mathrm{d}^2\vec{\xi}, \tag{68a}$$

$$\mathrm{HoT}_{\sigma_{xy}} = \int g^*C_x^*C_y^*\mathrm{d}^2\vec{\xi} + \mu^*\frac{\partial v^*}{\partial x}, \tag{68b}$$

$$\mathrm{HoT}_{q_x} = \int C_x^*(g^*C^{*,2} + h^*)\mathrm{d}^2\vec{\xi} + \kappa^*\frac{\partial T^*}{\partial x}. \tag{68c}$$

The unknown variables in Eq. (67) can be solved in a sequential manner: σ_{xx} from Eq. (67f), σ_{xy}, Eq. (67b), p, Eq. (67a), U_y, Eq. (67e), q_x, Eq. (67c), T, Eq. (67g), and ρ, Eq. (67d).

The velocity-space grid, spatial space grid and the reference variables are set the same as the Fourier flow cases. The Kn is defined as $\mathrm{Kn} = \sqrt{\pi}\mu_0 C_0/(2p_0L_0)$, and we consider the cases of Kn = 0.01, 0.1, 1 and 10. The convergence criterion for the DVM iteration is that the volume-weighted relative changes of temperature, density and velocity between two iterations must be less than 10^{-8},

$$E^k = \left.\frac{\sqrt{\sum_i(\psi_i^k - \psi_i^{k-1})^2\Delta x_i}}{\sqrt{\sum_i(\psi_i^{k-1})^2\Delta x_i}}\right|_{\max} < 1\times10^{-8}, \quad \text{for} \quad \psi\in\{\rho, T, v\}. \tag{69}$$

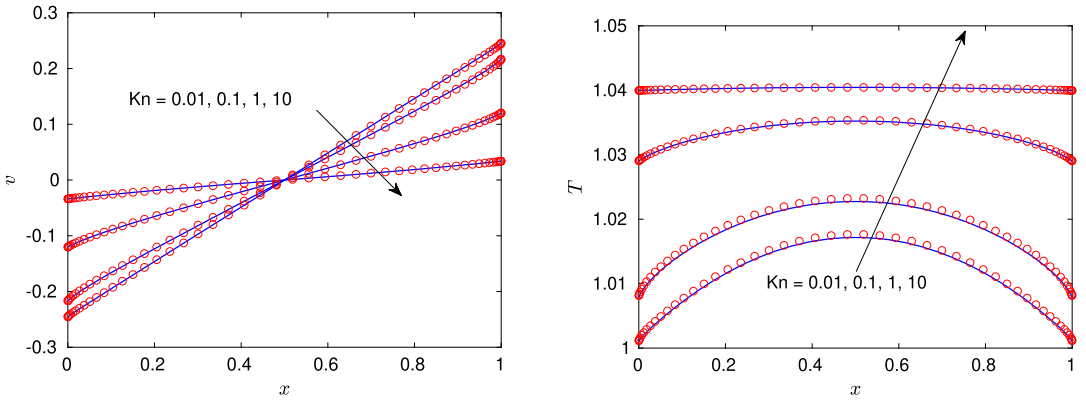

Fig. 5. Velocity (a) and temperature (b) profiles in the nonlinear Couette flow. The solid lines and circles represent the CIS and GSIS results, respectively.

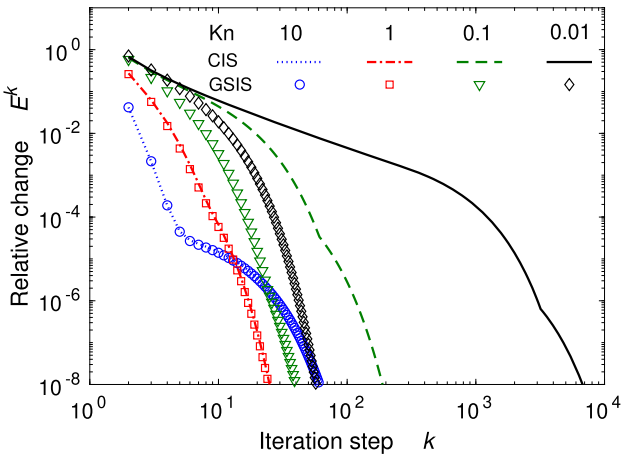

Fig. 6. Convergence history of both GSIS and CIS in the simulation of nonlinear Couette flow.

The converged velocity and temperature profiles predicted by GSIS and CIS are shown in Fig. 5, while the convergence history is shown in Fig. 6. It is seen that the GSIS converges in less than 70 steps for all the cases, while the CIS needs many more steps when Kn decreases to less than 0.1. For example, when Kn = 0.01, GSIS is faster than CIS by more than two orders.

5.4. Lid-driven cavity flow

This problem has been simulated extensively for validating gas kinetic schemes. The flow domain is a square cavity with a size of $L_0 \times L_0 = 1 \times 1$. The top boundary (the lid) of the cavity moves horizontally in the x direction with a velocity of $u_w = 0.14828$, while the other walls are fixed. All the solid walls are maintained at a uniform reference temperature of $T_w = 1$, where the Maxwellian diffuse boundary condition is applied, see Eq. (65).

The spatial space is discretized with Cartesian structured meshes and the gas kinetic equation is solved by the upwind finite difference scheme, while the macroscopic synthetic equations are solved using the implicit finite volume method described in Sec. 4.2. The cell centers are the finite difference nodes in the DVM discretization. The finite volume grid line positions are distributed according to

$$x_i, y_i = \frac{1}{2} + \frac{\tanh[a(i/N - 0.5)]}{2\tanh(a/2)}, \quad i = 0, 1, \ldots, N, \tag{70}$$

where N is the mesh size. The parameter a is adjusted such that the height of the first layer of cells adjacent to the wall is the set to desired value, i.e., $\Delta x_{\min} \equiv x_1 = y_1$. The convergence criterion for the DVM iteration is that the cell-volume averaged relative changes of all the conservative variables between two successive steps are less than 1×10^{-8}, i.e.,

$$E^k = \sqrt{\frac{\sum_{i,j}(\psi_{i,j}^k - \psi_{i,j}^{k-1})^2 \Omega_{i,j}}{\sum_{i,j}(\psi_{i,j}^{k-1})^2 \Omega_{i,j}}} < \epsilon_{\text{out}}, \quad \text{for} \quad \psi \quad \text{in} \quad \vec{W}. \tag{71}$$

Table 1
Number of DVM steps in CIS and GSIS and the overall CPU time for lid-driven cavity flow at different Knudsen numbers. Note that it takes 5 minutes to get the converged solution when the cavity flow is solved by the Navier-Stokes equations with no-slip boundary condition at Kn = 0.0002682.

Kn	Physical grid size	Velocity grid size	CIS: DVM steps	CIS: CPU time	GSIS: DVM steps	GSIS: CPU time
10	64×64	48×48	24	14 s	24	16 s
1	64×64	48×48	24	14 s	23	29 s
0.075	64×64	28×28	226	40 s	52	2.2 min
0.002682	128×128	28×28	40, 917	123 min	234	10.5 min
0.0002682	128×128	28×28	1, 283, 068	64.2 h	1410	49 min

The convergence criterion of solving the macroscopic synthetic equations (the inner loop) is defined exactly the same as the outer loop, but with the superscript k changed to n, and ϵ_{out} changed to ϵ_{in}. For this flow problem, $\epsilon_{\text{out}} = 1 \times 10^{-8}$ and $\epsilon_{\text{in}} = 1 \times 10^{-6}$.

We first consider the rarefied gas flows, with Kn = 0.075, 1 and 10. The physical space grid is set as $N = 64$ and $\Delta x_{\min} = 5 \times 10^{-3}$. For Kn = 1 and 10, the velocity-space grid is set according to Eq. (62), with $N_V = 48$. While for the case of Kn = 0.075, we use a 28-by-28-point velocity grid with the half-range Gauss-Hermite quadrature. The macroscopic synthetic equations are solved in the domain excluding four layers of cells adjacent to the solid walls. Comparisons of temperature and heat flux streamlines are shown in Fig. 7, and the velocity profiles across the center lines of the cavity are shown in Fig. 8. These figures show that in the rarefied regime, the GSIS and CIS results match well with each other, and both schemes capture the anti-Fourier heat transfer phenomenon (from cold to hot) at the top right corner even Kn is as small as 0.075.

For flows in the near-continuum regime, we consider the case of Re = 100 and Re = 1000, corresponding to Kn = 2.628×10^{-3} and 2.628×10^{-4}, respectively. The spatial grids are set as $N = 64$, $\Delta x_{\min} = 5 \times 10^{-3}$ when Re = 100 and $N = 128$, $\Delta x_{\min} = 2 \times 10^{-3}$ when Re = 1000. The velocity grids are set the same as the case of Kn = 0.075. Fig. 9 shows the velocity streamlines predicted by GSIS. The vortex patterns, including size and vortex center positions, agree with the reported results [49]. To get a more quantitative comparison, in Fig. 10 we plot the velocity profiles on the vertical and horizontal centerlines of the cavity, predicted by both CIS and GSIS, together with Ghia's benchmark solution [49]. We can see that, when Re = 100, CIS and GSIS predicted almost the same solutions, and both agree well with the benchmark solution. When Re = 1000, there is a slight difference between the GSIS and CIS results.

The comparison of the convergence history of the DVM iteration is shown in Fig. 11 for both the rarefied and continuum flow cases. The corresponding CPU time and the number of DVM steps in both CIS and GSIS are listed in Table 1. The serial Fortran program is compiled using the Intel Fortran compiler (version 19.1.1) with the "-xHost" option, and runs on the Intel© Xeon© Gold 5118 CPU@2.3 GHz. We can see that for the cases of Kn = 1 and 10, the convergence history of CIS and GSIS is very similar, both converge in after about 23 DVM steps. Due to the additional cost in solving the macroscopic synthetic equations, with the same number of DVM steps the overall computing cost of GSIS is higher for these highly rarefied cases. However, when Kn ≤ 0.075, GSIS needs significantly fewer DVM steps than CIS, e.g., when Re = 100, GSIS achieves convergence after 234 DVM steps, while CIS becomes extremely expensive. For these low Kn cases, because GSIS can reduce the number of DVM steps by several orders, the additional cost for solving the macroscopic synthetic equations is negligible.

5.5. Supersonic flow past a circular cylinder

The last testing case is the supersonic rarefied gas flow passing a circular cylinder. The 2D flow domain is an annulus with the inner circle with radius r_{in} being the cylinder surface, and the outer circle with radius of $r_{\text{out}} = 11 r_{\text{in}}$ being the far-field boundary. The free-stream Mach number is Ma_∞. The cylinder surface temperature is set as the same as the free-stream temperature $T_{\text{w}} = T_\infty$. To properly compare with the reported results [23,25], the Knudsen number is defined as

$$\text{Kn} = \frac{(5 - 2\omega)(7 - 2\omega)\mu_\infty C_\infty}{15\sqrt{\pi}\, p_\infty r_{\text{in}}} \tag{72}$$

where μ_∞, C_∞ and p_∞ are the viscosity, the most probable molecular velocity and the pressure at the free-stream condition, respectively.

Due to symmetry, only the upper-half domain is computed and the symmetric boundary condition is applied. The physical grid size is $M \times N$, where M is the number of cells along the upper surface of the cylinder and N is the number of cells along the radial direction. The cell height along the radial direction grows with a constant expansion ratio from the first layer's height ($\Delta r_{\min}$). The cell width along the cylinder surface grows from leading and trailing edges of the cylinder toward the upper position with a constant expansion ratio, such that the largest cell width is five times of the smallest one. For the cases of Kn = 1 and 0.1, the physical grid is set as $N = 50$, $M = 64$ and $\Delta r_{\min} = 0.01$, while for the case of Kn = 0.01, $N = 80$, $M = 80$ and $\Delta r_{\min} = 0.001$. The discrete velocity set is a uniform Cartesian grid with 90^2 points in the range

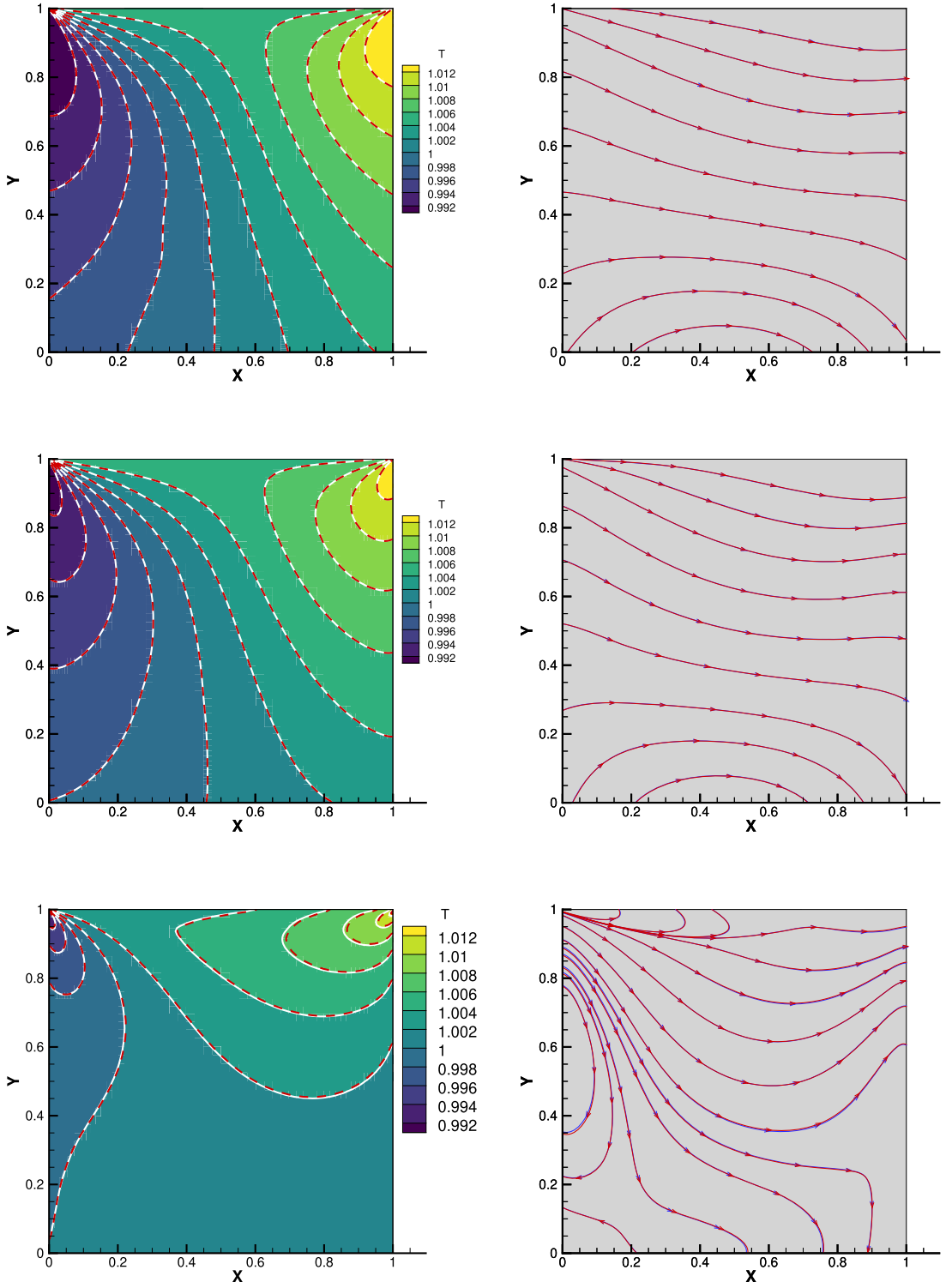

Fig. 7. Contours of the temperature field (left) and streamlines of the heat flux field (right) for the cavity flow with Kn = 10 (top), 1 (middle) and 0.075 (bottom). In the temperature contours, the CIS results are shown in colored background with white lines, while the GSIS results are shown as dashed red lines. In the streamline plots, the CIS and GIS results are denoted by the blue and red lines, respectively. (For interpretation of the colors in the figure(s), the reader is referred to the web version of this article.)

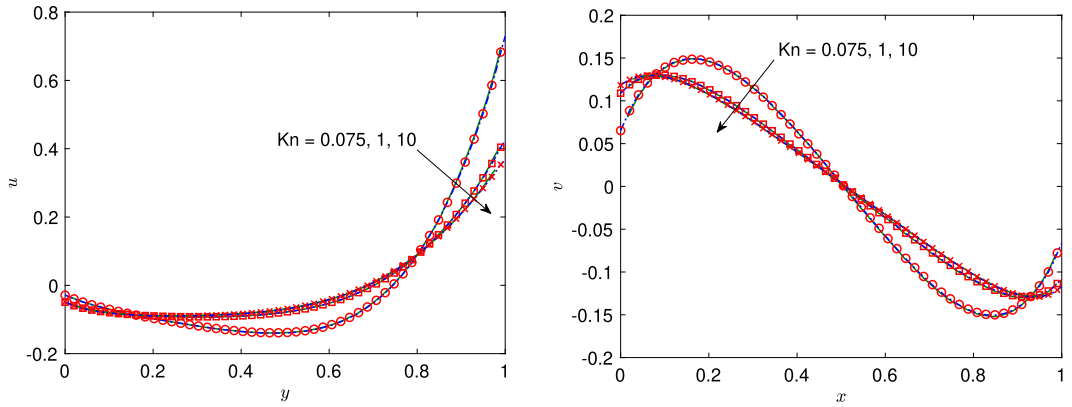

Fig. 8. Profiles of the horizontal (left) and vertical (right) velocity components along the vertical/horizontal center lines of the cavity. Along the arrow, the Knudsen numbers corresponding to the lines are 0.075, 1 and 10, respectively. The solid green lines are the results extracted from Ref. [23] which are computed with the explicit discrete-UGKS. The blue lines and red markers represent the CIS and GSIS results, respectively.

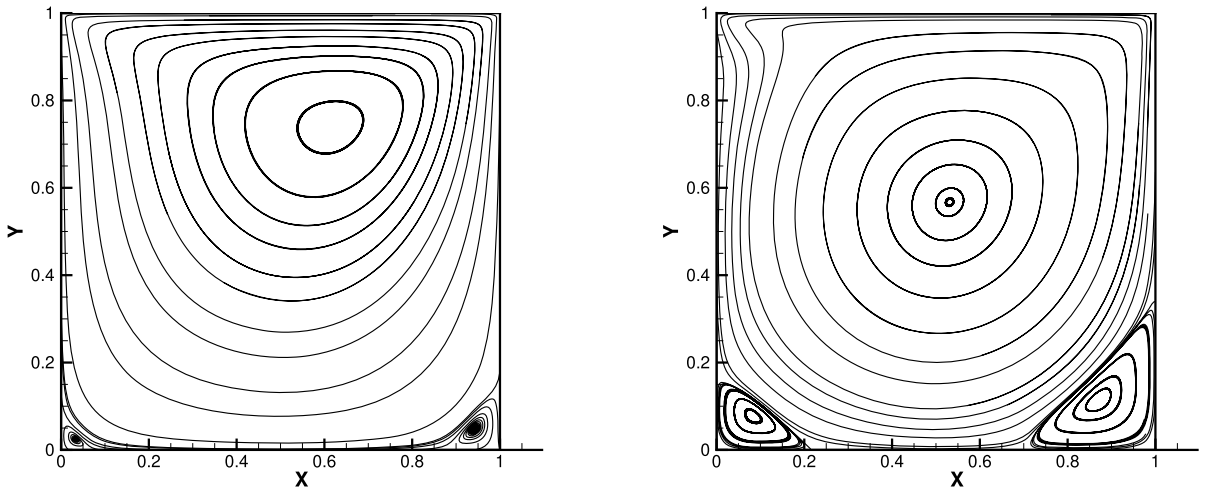

Fig. 9. The streamlines of velocity for the lid-driven cavity flow at Re = 100 (left) and 1000 (right).

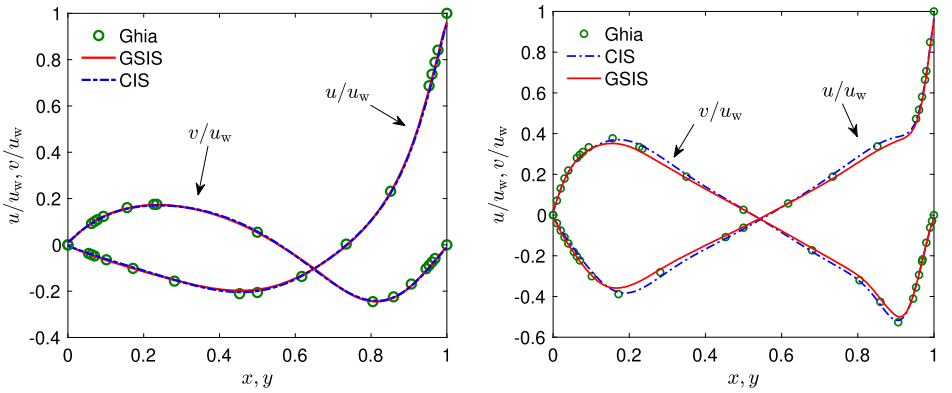

Fig. 10. The profiles of normalized horizontal (vertical) velocity components u (v) on the vertical (horizontal) central lines of the cavity. Left: Re = 100; Right: Re = 1000.

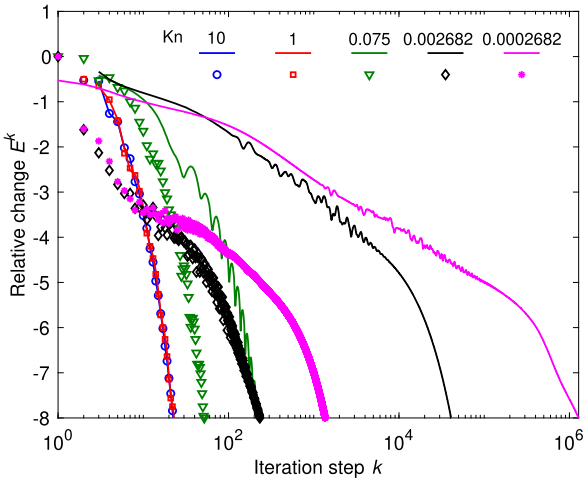

Fig. 11. Convergence history of the cavity flow at different Knudsen numbers. Solid lines and markers represent results of CIS and GSIS, respectively.

Table 2
Number of DVM steps in CIS and GSIS and the overall CPU time for the supersonic cylinder flow.

Kn	Physical grid size	Velocity grid size	CIS: DVM steps	CIS: CPU time	GSIS: DVM steps	GSIS: CPU time
1	64×50	90×90	186	12 min	264	27 min
0.1	64×50	90×90	552	36 min	232	24 min
0.01	80×80	90×90	4,925	508 min	210	42 min

of $[-15, 15]^2$. The DVM method is implemented using the implicit time-stepping scheme as described in Sec. 4.1. The CFL number in the DVM and NS solvers are 1000 and 100, respectively. The convergence criterion of the outer loop and inner loop in Eq. (71) are set as $\epsilon_{\text{out}} = 1 \times 10^{-6}$ and $\epsilon_{\text{in}} = 1 \times 10^{-6}$.

Fig. 12 presents the temperature and local Mach number contours of the results predicted by GSIS and CIS, which are overlapped with the literature results wherever available, in particular the DSMC and discrete-UGKS solutions [23]. We can observe good agreement between the CIS and GSIS solutions, and overall good matches with the results reported in literature. Fig. 13 shows the pressure (normal stress), shear stress and heat flux along the upper surface of the cylinder. Comparisons are made with the results from the literature including Refs. [23] and [25]. Again, it is shown that current GSIS results agree well with the reported results. In the bottom of Fig. 13, it is seen that both GSIS and CIS capture the flow separation from the surface precisely at the same location around 153°.

To assess the efficiency of GSIS, we plot the convergence history of the DVM steps in both GSIS and CIS in Fig. 14. In addition, Table 2 lists the number of DVM steps and overall computing time in the same environment as in the lid-driven cavity flow. Obviously, for highly rarefied flows, CIS is very efficient: when Kn = 1, the solution converges after 186 steps and the total computing time is around 12 minutes. For this case, GSIS needs more DVM steps than the CIS, and the overall computing time is about twice of CIS. As Kn decreases to 0.1, GSIS becomes slightly more efficient than CIS. When Kn = 0.01, CIS requires as many as 4925 DVM steps and needs around 8 hours to reach convergence, while GSIS takes only 42 minutes and converges within 210 DVM steps. We note that for small-Kn cases, the inner loop solving the macroscopic synthetic equations also takes much fewer time steps to converge, because in these case the Reynolds numbers are much higher, favoring a fast convergence of the NSF solver.

6. Conclusions

In summary, we have extended GSIS to find steady-state solutions of the nonlinear gas kinetic equation, which couples a simple iterative scheme to solve the gas kinetic equation with an implicit scheme to solve the macroscopic synthetic equations. Unlike the pure DVM schemes, GSIS enables the DVM simulation to converge very quickly in the near-continuum flow regime, which is realized by solving the macroscopic synthetic equations to the steady state after each DVM iteration. The viscous fluxes of the macroscopic synthetic equations explicitly include the NSF constitutive relation, while the higher-order terms are calculated directly from the velocity distribution function available after each DVM step. Such a treatment guarantees the accuracy of GSIS in both the continuum and rarefied regimes. In addition, the construction of higher-order terms is further simplified in this paper, compared with the linear GSIS [28]. Several classical cases have been used to analyze accuracy and efficiency of the nonlinear GSIS, based on the Shakhov kinetic model. The numerical results demonstrate that our scheme is able to obtain steady-state solutions of the gas kinetic equation in a relatively smaller number of iterations.

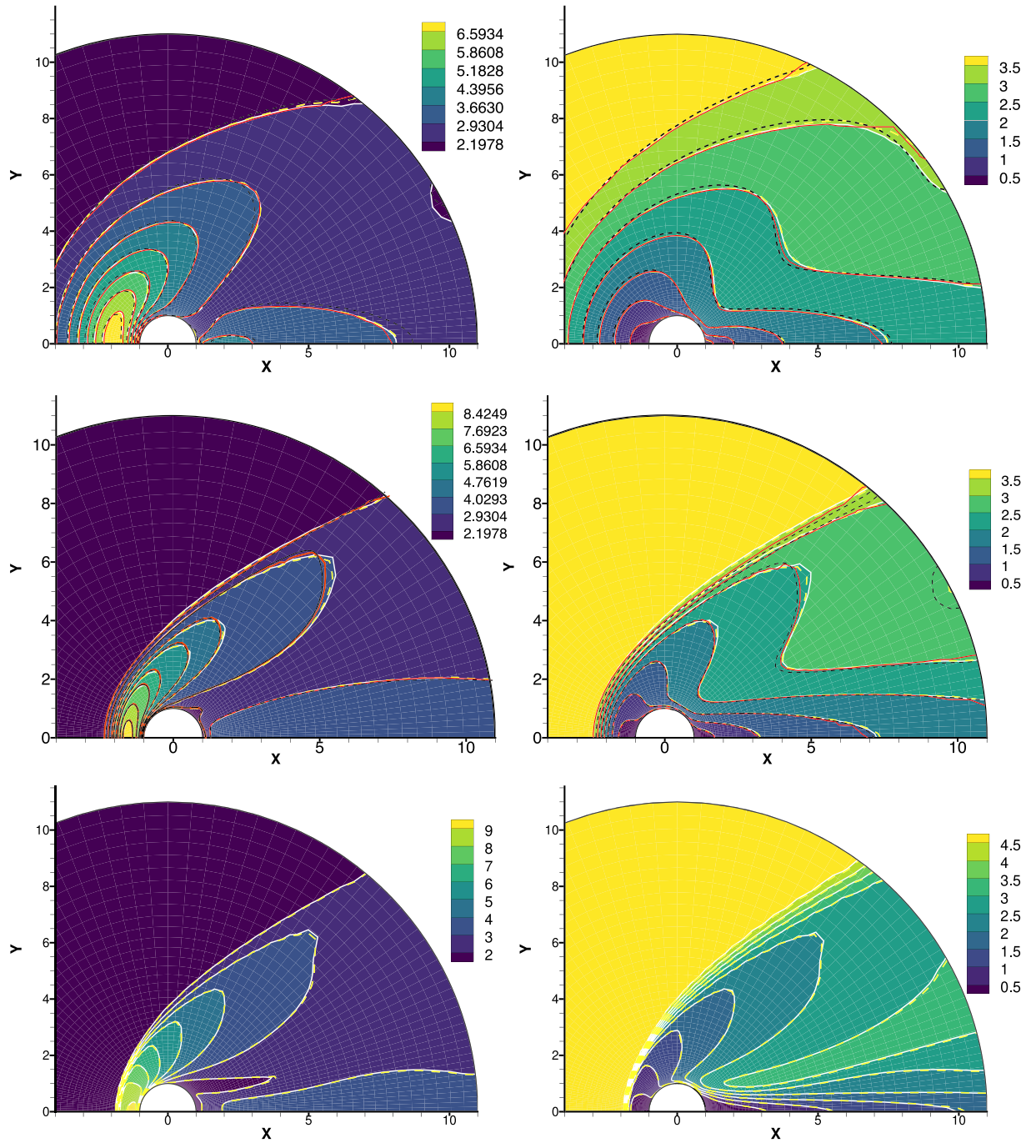

Fig. 12. Cylinder flow at $Ma_\infty = 5$ and (top) Kn = 1, (middle) Kn=0.1, (bottom) Kn=0.01: comparison of the non-dimensional temperature (left) and local Mach number (right) fields obtained by CIS and GSIS, together with the reference discrete-UGKS and DSMC solutions extracted from Ref. [23]. The GSIS results are indicated by the colored background with white solid lines, the CIS solutions are presented by the dashed yellow lines. The discrete-UGKS and DSMC solutions are represented by the solid red lines and dashed black lines, respectively.

For high-speed flows, GSIS also shows a significant speed-up in comparison with the conventional iteration scheme for low-Kn flows.

Compared to the implicit unified gas kinetic scheme and its improved versions [25,50], GSIS does not rely on the relaxation time approximation of the Boltzmann collision operator, thus like the linear GSIS [28], it can be extended to solve the full Boltzmann equation. Actually, the simple construction of high-order terms proposed in this work further enhances the potential of GSIS to account for multi-species and vibrational non-equilibrium phenomena, which are critical for high-speed rarefied gas flows such as the re-entry space engineering. In the future work we will use multi-block or unstructured-mesh

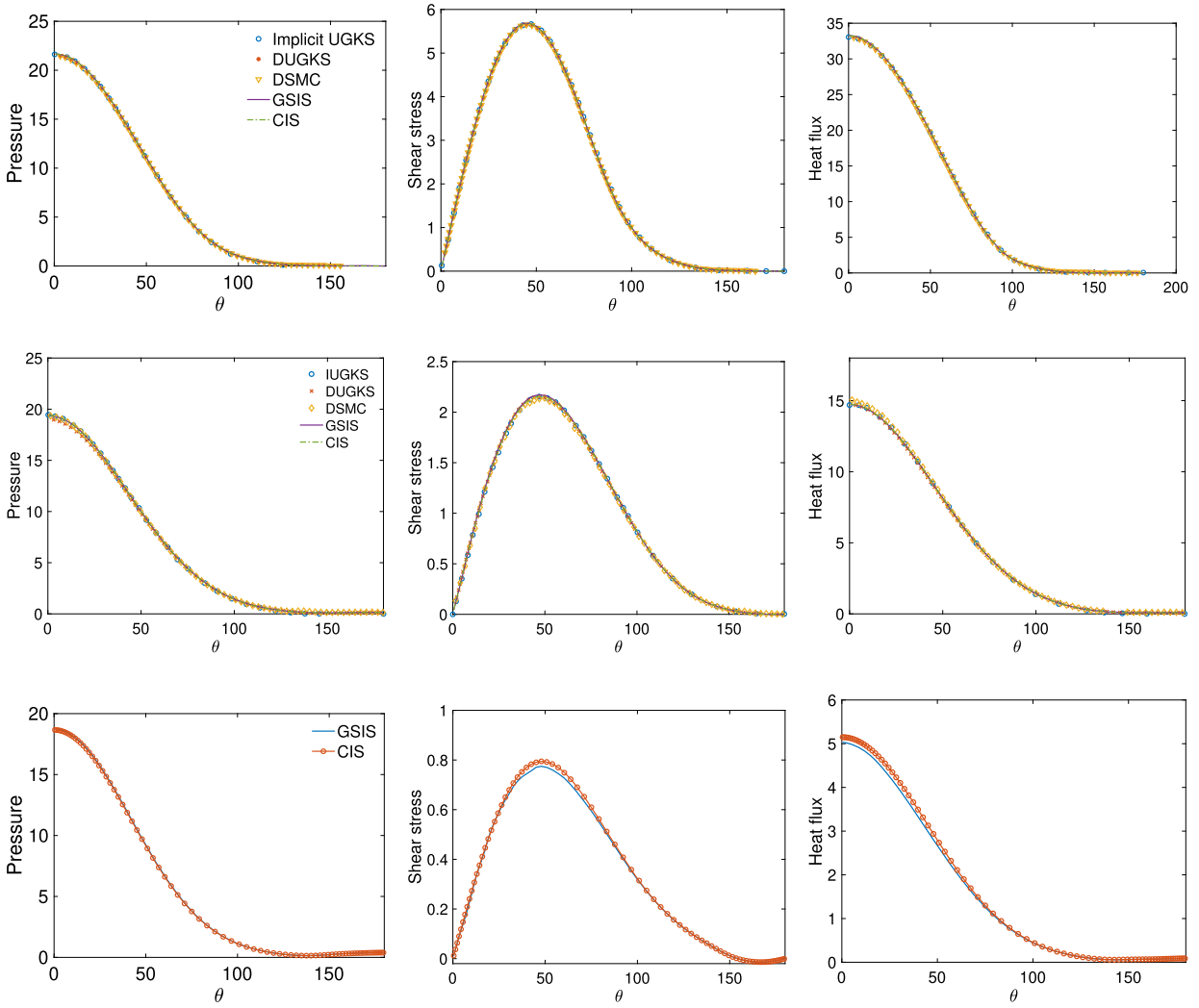

Fig. 13. Comparison of the surface quantities on the cylinder, when (top) Kn = 1, (middle) Kn=0.1, and (bottom) Kn=0.01. The discrete-UGKS and DSMC data are extracted from Ref. [23]. The implicit UGKS data are extracted from Ref. [25]. The X-axis is the angle (°) from leading edge of the cylinder.

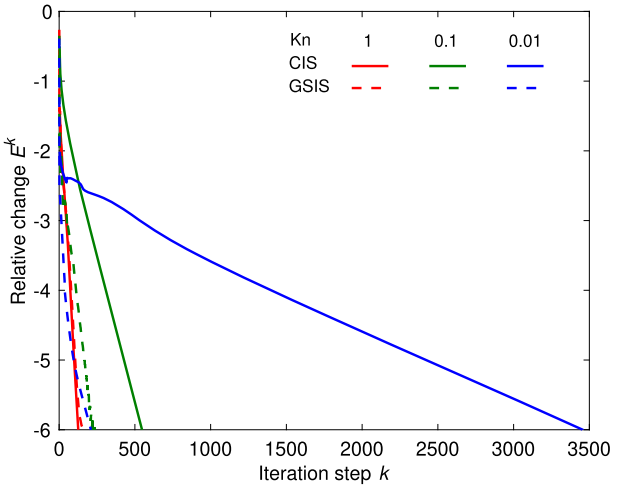

Fig. 14. Convergence history of the DVM time stepping in the supersonic cylinder flow at different Knudsen number. The red, green and blue lines are for Kn = 1, 0.1 and 0.01, respectively. The solid and dashed lines represent the CIS and GSIS results, respectively.

techniques to extend GSIS for more practical three-dimensional flows with irregular geometries. We will also investigate the possibility of coupling the new macroscopic synthetic equations with DSMC, i.e. to produce a DSMC-GSIS algorithm to remove the restriction on cell size and reduce the computing cost for low-Kn flows.

CRediT authorship contribution statement

L.H. Zhu: Conceptualization of scheme II, Coding and writing. **X.C. Pi:** Conceptualization of scheme II. **W. Su:** Conceptualization of scheme I. **L. Wu:** Conceptualization of scheme I, Methodology: calculation of the convergence rate, Supervision and writing. **Z.H. Li:** Supervision and writing. **Y.H. Zhang:** Supervision and writing.

Declaration of competing interest

The authors declare that they have no known competing financial interests or personal relationships that could have appeared to influence the work reported in this paper.

Acknowledgements

L. Zhu acknowledges the financial support of European Union's Horizon 2020 Research and Innovation Programme under the Marie Skłodowska-Curie grant agreement number 793007. Financial support in the UK by the Engineering and Physical Sciences Research Council under grants EP/R041938/1, EP/M021475/1, and EP/R029581/1, and in China by the projects of manned space engineering technology (2018-14) "Development of spacecraft flight and reentry monitoring and forecasting system" and the National Natural Science Foundation of China (91530319) are greatly acknowledged.

References

[1] Z. Li, A. Peng, Q. Ma, L. Dang, X. Tang, X. Sun, Gas-kinetic unified algorithm for computable modeling of Boltzmann equation and application to aerothermodynamics for falling disintegration of uncontrolled Tiangong-no. 1 spacecraft, Adv. Aerodyn. 1 (2019) 1–21.
[2] A. Viviani, A. Aprovitola, L. Iuspa, G. Pezzella, Aeroshape design of reusable re-entry vehicles by multidisciplinary optimization and computational fluid dynamics, Aerosp. Sci. Technol. 105 (2020) 106029.
[3] S. Chapman, T.G. Cowling, The Mathematical Theory of Non-Uniform Gases: An Account of the Kinetic Theory of Viscosity, Thermal Conduction and Diffusion in Gases, Cambridge University Press, 1970.
[4] H. Grad, On the kinetic theory of rarefied gases, Commun. Pure Appl. Math. 2 (1949) 331–407, https://doi.org/10.1002/cpa.3160020403.
[5] H. Struchtrup, Macroscopic Transport Equations for Rarefied Gas Flows, Approximation Methods in Kinetic Theory, Springer, 2006, https://www.springer.com/gp/book/9783540245421.
[6] X.-J. Gu, D.R. Emerson, A high-order moment approach for capturing non-equilibrium phenomena in the transition regime, J. Fluid Mech. 636 (2009) 177, https://doi.org/10.1017/s002211200900768x.
[7] V.V. Aristov, Direct Methods for Solving the Boltzmann Equation and Study of Nonequilibrium Flows, Springer Science & Business Media, 2001, https://www.springer.com/gp/book/9780792368311.
[8] G.A. Bird, Molecular Gas Dynamics and the Direct Simulation of Gas Flows, Clarendon Press, 1994.
[9] W. Wagner, A convergence proof for Bird's direct simulation Monte Carlo method for the Boltzmann equation, J. Stat. Phys. 66 (1992) 1011–1044, https://doi.org/10.1007/bf01055714.
[10] Z. Li, M. Fang, X. Jiang, J. Wu, Convergence proof of the DSMC method and the gas-kinetic unified algorithm for the Boltzmann equation, Sci. China, Phys. Mech. Astron. 56 (2013) 404–417, https://doi.org/10.1007/s11433-013-4999-3.
[11] P. Wang, M.T. Ho, L. Wu, Z. Guo, Y. Zhang, A comparative study of discrete velocity methods for low-speed rarefied gas flows, Comput. Fluids 161 (2018) 33–46, https://doi.org/10.1016/j.compfluid.2017.11.006.
[12] S. Chen, K. Xu, A comparative study of an asymptotic preserving scheme and unified gas-kinetic scheme in continuum flow limit, J. Comput. Phys. 288 (2015) 52–65, https://doi.org/10.1016/j.jcp.2015.02.014.
[13] T.E. Schwartzentruber, L.C. Scalabrin, I.D. Boyd, A modular particle–continuum numerical method for hypersonic non-equilibrium gas flows, J. Comput. Phys. 225 (2007) 1159–1174, https://doi.org/10.1016/j.jcp.2007.01.022.
[14] I.D. Boyd, T.R. Deschenes, Hybrid Particle-Continuum Numerical Methods for Aerospace Applications, Tech. Rep., Michigan Univ Ann Arbor Dept of Aerospace Engineering, Jan. 2011, https://apps.dtic.mil/docs/citations/ADA588168.
[15] A. Alaia, G. Puppo, A hybrid method for hydrodynamic-kinetic flow - part II - coupling of hydrodynamic and kinetic models, J. Comput. Phys. 231 (2012) 5217–5242, https://doi.org/10.1016/j.jcp.2012.02.022.
[16] Z.H. Li, Z.H. Li, H.Y. Li, Y.G. Yang, Application of hybrid N-S/DSMC method in hypersonic transitional flow, in: 28th International Symposium on Rarefied Gas Dynamics 2012, vols. 1 and 2, in: AIP Conference Proceedings, vol. 1501, 2012, pp. 435–442.
[17] M. Darbandi, E. Roohi, A hybrid DSMC/Navier-Stokes frame to solve mixed rarefied/nonrarefied hypersonic flows over nano-plate and micro-cylinder, Int. J. Numer. Methods Fluids 72 (2013) 937–966, https://doi.org/10.1002/Fld.3769.
[18] W. Yang, X.-J. Gu, L. Wu, D.R. Emerson, Y. Zhang, S. Tang, A hybrid approach to couple the discrete velocity method and method of moments for rarefied gas flows, J. Comput. Phys. 410 (2020) 109397, https://doi.org/10.1016/j.jcp.2020.109397.
[19] K. Xu, J.-C. Huang, A unified gas-kinetic scheme for continuum and rarefied flows, J. Comput. Phys. 229 (2010) 7747–7764, https://doi.org/10.1016/j.jcp.2010.06.032.
[20] K. Xu, J.C. Huang, An improved unified gas-kinetic scheme and the study of shock structures, IMA J. Appl. Math. 76 (2011) 698–711, https://doi.org/10.1093/imamat/hxr002.
[21] Z. Guo, K. Xu, R. Wang, Discrete unified gas kinetic scheme for all Knudsen number flows: low-speed isothermal case, Phys. Rev. E 88 (2013) 033305, https://doi.org/10.1103/PhysRevE.88.033305.
[22] Z. Guo, R. Wang, K. Xu, Discrete unified gas kinetic scheme for all Knudsen number flows, II: thermal compressible case, Phys. Rev. E 91 (2015) 033313, https://doi.org/10.1103/PhysRevE.91.033313.
[23] L. Zhu, Z. Guo, K. Xu, Discrete unified gas kinetic scheme on unstructured meshes, Comput. Fluids 127 (2016) 211–225, https://doi.org/10.1016/j.compfluid.2016.01.006.

[24] Z. Guo, J. Li, K. Xu, On unified preserving properties of kinetic schemes, arXiv:1909.04923.
[25] Y. Zhu, C. Zhong, K. Xu, Implicit unified gas-kinetic scheme for steady state solutions in all flow regimes, J. Comput. Phys. 315 (2016) 16–38, https://doi.org/10.1016/j.jcp.2016.03.038.
[26] Y. Zhu, C. Zhong, K. Xu, Unified gas-kinetic scheme with multigrid convergence for rarefied flow study, Phys. Fluids 29 (2017) 096102, https://doi.org/10.1063/1.4994020.
[27] D. Jiang, M. Mao, J. Li, X. Deng, An implicit parallel UGKS solver for flows covering various regimes, Adv. Aerodyn. 1 (2019) 8, https://doi.org/10.1186/s42774-019-0008-5.
[28] W. Su, L. Zhu, P. Wang, Y. Zhang, L. Wu, Can we find steady-state solutions to multiscale rarefied gas flows within dozens of iterations?, J. Comput. Phys. 407 (2020) 109245, https://doi.org/10.1016/j.jcp.2020.109245.
[29] M.L. Adams, E.W. Larsen, Fast iterative methods for discrete-ordinates particle transport calculations, Prog. Nucl. Energy 40 (2002) 3–159, https://doi.org/10.1016/S0149-1970(01)00023-3.
[30] D. Valougeorgis, S. Naris, Acceleration schemes of the discrete velocity method: gaseous flows in rectangular microchannels, SIAM J. Sci. Comput. 25 (2003) 534–552, https://doi.org/10.1137/S1064827502406506.
[31] J. Lihnaropoulos, S. Naris, D. Valougeorgis, Formulation and stability analysis of rapidly convergent iteration schemes for the 2-D linearized BGK equation, Transp. Theory Stat. Phys. 36 (2007) 513–528, https://doi.org/10.1080/00411450701468415.
[32] L. Szalmás, D. Valougeorgis, A fast iterative model for discrete velocity calculations on triangular grids, J. Comput. Phys. 229 (2010) 4315–4326, https://doi.org/10.1016/j.jcp.2010.02.015.
[33] L. Szalmás, Accelerated discrete velocity method for axial-symmetric gaseous flows, Comput. Phys. Commun. 184 (2013) 1432–1438, https://doi.org/10.1016/j.cpc.2013.01.011.
[34] L. Szalmás, An accelerated discrete velocity method for flows of rarefied ternary gas mixtures in long rectangular channels, Comput. Fluids 128 (2016) 91–97, https://doi.org/10.1016/j.compfluid.2016.01.010.
[35] L. Wu, J. Zhang, H. Liu, Y. Zhang, J.M. Reese, A fast iterative scheme for the linearized Boltzmann equation, J. Comput. Phys. 338 (2017) 431–451, https://doi.org/10.1016/j.jcp.2017.03.002.
[36] W. Su, P. Wang, H. Liu, L. Wu, Accurate and efficient computation of the Boltzmann equation for Couette flow: influence of intermolecular potentials on Knudsen layer function and viscous slip coefficient, J. Comput. Phys. 378 (2018) 573–590, https://doi.org/10.1016/j.jcp.2018.11.015.
[37] W. Su, M.T. Ho, Y. Zhang, L. Wu, GSIS: an efficient and accurate numerical method to obtain the apparent gas permeability of porous media, Comput. Fluids 22 (2020), https://doi.org/10.13140/RG.2.2.10728.21762.
[38] D. Pan, C. Zhong, C. Zhuo, An implicit discrete unified gas-kinetic scheme for simulations of steady flow in all flow regimes, Commun. Comput. Phys. 25 (2019), https://doi.org/10.4208/cicp.OA-2017-0262.
[39] E.M. Shakhov, Generalization of the Krook kinetic relaxation equation, Fluid Dyn. 3 (1968) 95–96, https://doi.org/10.1007/BF01029546.
[40] W. Su, P. Wang, Y. Zhang, L. Wu, Implicit discontinuous Galerkin method for the Boltzmann equation, J. Sci. Comput. 82 (2020) 39, https://doi.org/10.1007/s10915-020-01139-7.
[41] M.T. Ho, L. Zhu, L. Wu, P. Wang, Z. Guo, Z.-H. Li, Y. Zhang, A multi-level parallel solver for rarefied gas flows in porous media, Comput. Phys. Commun. 234 (2019) 14–25, https://doi.org/10.1016/j.cpc.2018.08.009.
[42] L. Zhu, P. Wang, S. Chen, Z. Guo, Y. Zhang, GPU acceleration of an iterative scheme for gas-kinetic model equations with memory reduction techniques, Comput. Phys. Commun. 245 (2019) 106861, https://doi.org/10.1016/j.cpc.2019.106861.
[43] W. Su, L.H. Zhu, L. Wu, Fast convergence and asymptotic preserving of the general synthetic iterative scheme, SIAM J. Sci. Comput. 42 (2020) B1517–B1540, https://doi.org/10.1137/20M132691X.
[44] Z.-H. Li, H.-X. Zhang, Study on gas kinetic unified algorithm for flows from rarefied transition to continuum, J. Comput. Phys. 193 (2004) 708–738, https://doi.org/10.1016/j.jcp.2003.08.022.
[45] A.-P. Peng, Z.-H. Li, J.-L. Wu, X.-Y. Jiang, Implicit gas-kinetic unified algorithm based on multi-block docking grid for multi-body reentry flows covering all flow regimes, J. Comput. Phys. 327 (2016) 919–942, https://doi.org/10.1016/j.jcp.2016.09.050.
[46] J. Blazek, Computational Fluid Dynamics: Principles and Applications, Butterworth-Heinemann, 2015.
[47] J. Meng, N. Dongari, J.M. Reese, Y. Zhang, Breakdown parameter for kinetic modeling of multiscale gas flows, Phys. Rev. E 89 (2014) 063305, https://doi.org/10.1103/PhysRevE.89.063305.
[48] L. Wu, J.M. Reese, Y. Zhang, Solving the Boltzmann equation deterministically by the fast spectral method: application to gas microflows, J. Fluid Mech. 746 (2014) 53–84, https://doi.org/10.1017/jfm.2014.79.
[49] U. Ghia, K.N. Ghia, C.T. Shin, High-Re solutions for incompressible flow using the Navier-Stokes equations and a multigrid method, J. Comput. Phys. 48 (1982) 387–411, https://doi.org/10.1016/0021-9991(82)90058-4.
[50] L.M. Yang, C. Shu, W.M. Yang, Z. Chen, H. Dong, An improved discrete velocity method (DVM) for efficient simulation of flows in all flow regimes, Phys. Fluids 30 (2018) 062005, https://doi.org/10.1063/1.5039479.